https://doi.org/10.5194/egusphere-2026-5345
Preprint. Discussion started: 23 September 2026

Assessing the use of satellite products from multispectral unmixing and differential interferometry for Altay snow water equivalent estimation

Yiwen Fang[1], Jinmei Pan[2], Steven A. Margulis[3], Jingtian Zhou[2], Haorui Sun[3], Yang Lei[4], Chuan Xiong[4], Hua Wang[5], Shurun Tan[1,6,7,8]*

[1]Zhejiang University-University of Illinois Urbana-Champaign Institute, Zhejiang University, Haining, Zhejiang 314400, China
[2]National Space Science Center, Chinese Academy of Sciences, Beijing 100190, China
[3]Department of Civil and Environmental Engineering, University of California, Los Angeles, Los Angeles, CA 90095, USA
[4]Southwest Jiaotong University, Chengdu, Sichuan 611756, China
[5]International Business School, Zhejiang University, Haining, Zhejiang 314400, China
[6]State Key Laboratory of Extreme Photonics and Instrumentation, Zhejiang University, Hangzhou, Zhejiang 310027, China
[7]Zhejiang Key Laboratory of Intelligent Electromagnetic Control and Advanced Electronic Integration, Zhejiang University, Hangzhou, Zhejiang 310027, China
[8]College of Information Science and Electronic Engineering, Zhejiang University, Hangzhou, Zhejiang 310027, China

Correspondence to: Shurun Tan (srtan@intl.zju.edu.cn)

Abstract. This work evaluates the application of fractional snow covered area (fSCA) derived from Harmonized Landsat Sentinel (HLS) multi-spectral images and snow products derived from Sentinel-1 and LuTan-1 interferometric Synthetic Aperture Radar (InSAR) pairs, in generating snow water equivalent (SWE) at the Kelan watershed in Altay, northwestern China. The newly retrieved HLS fSCA was first assimilated using a previously-developed snow reanalysis framework to generate daily SWE estimates at a spatial resolution of ~ 150 m over Water Years (WYs) 2018 – 2025. The snow reanalysis dataset is verified against an in situ SWE site, in situ snow depth sites and Uncrewed Aerial Vehicle (UAV) Lidar swaths. The 8-year average peak SWE volume estimated from the fSCA constrained dataset is ~ 0.76 km^3, 35% of which is distributed at elevations above 1500 m. Based on the snow reanalysis dataset, SWE increases by more than 0.02-0.03 m (corresponding to a 2π wrapping cycle in C band) over a 12-day period at over ~20% of the pixel-time samples in most of the years, likely to be affected by phase wrapping in C-band InSAR retrievals. The likelihood is reduced for L-band retrievals over a 12-day measurement period. Residual phase ambiguity remains in the Sentinel-1 ΔSWE retrievals, with more than 10% of observations requiring at least one 2π cycle to match the reanalysis reference. Verification at the in situ site shows that even a single ΔSWE retrieval affected by phase wrapping can reduce the accuracy of SWE estimates using the current snow reanalysis framework. After resolving the phase wrapping in Sentinel-1 ΔSWE retrievals at the in situ SWE site, SWE generated from adjusted ΔSWE assimilation shows comparable performance to SWE from HLS fSCA assimilation in WYs 2020 and 2021. In WY 2024, however, LuTan-1 ΔSWE assimilation yields a higher unbiased root mean square difference despite negligible phase-wrapping issues, because ΔSWE retrievals are only available on low-accumulation days. The overall limited effectiveness of InSAR ΔSWE assimilation may be partly related to the scarcity of high-quality InSAR observations compared

https://doi.org/10.5194/egusphere-2026-5345
Preprint. Discussion started: 23 September 2026

to fSCA observations, Sentinel-1's relatively long revisit interval, and a data-assimilation approach not ideally suited to ΔSWE observations. Future work should develop assimilation methods that explicitly account for phase-cycle uncertainty, allowing a more rigorous assessment of how well C-band retrievals constrain modeled SWE. Assimilation performance should also be evaluated with high-quality retrievals from upcoming low-frequency (L- and P-band) InSAR missions.

1 Introduction

In mountainous regions of northwestern China, snow serves as the main water source for agricultural, fisheries, and animal husbandry, as well as a critical resource for tourism. For example, in the Altay prefecture, more than 90% of the fresh water supply is used in industrial applications, contributing to ~15% to 20% of the total GDP. Applications related to ice and snow tourism have thrived since 2015, taking up over 40% of the total GDP recently (Yang et al., 2025). Accurate knowledge of snow amount and timing in Altay, as well as its vulnerability to climate change, is essential for human use and the local economy.

Due to the high uncertainty of meteorological forcings and intensive computational requirements, there are few or no snow datasets at sub-kilometer spatial resolution in mountainous areas in northwestern China, making it an understudied region. At the Kelan watershed in Altay, there is only one publicly available meteorological station measuring snow depth located at a low elevation of less than 1000 m. Recent snow surveys primarily focus on evaluating the impact of snow microstructure or soil properties on estimated brightness temperature and backscatter from microwave scattering models (Dai et al., 2022; Xiong et al., 2022). Although globally distributed coarse-resolution snow datasets such as ERA5-Land (Muñoz-Sabater et al., 2021), GLDAS (Rodell et al., 2004), and JRA55 (Kobayashi et al., 2015) are available, their uncertainties are typically high are typically high in regions with limited in situ measurements (Liu et al., 2022). Large uncertainties are observed in snow depth and SWE estimated from land surface models (You et al., 2023) in the melting season without observational constraints. Therefore, a regional space-time continuous SWE dataset at sub-kilometer resolution is needed to quantify water volume in Altay and used serve as a benchmark for evaluating new snow products.

Assimilation of fractional snow covered area (fSCA) from optical sensors has been verified as a promising tool to generate SWE at sub-kilometer spatial resolution (Margulis et al., 2016; Liu et al., 2021; Fang et al., 2022). Given that fSCA values tend to saturate at 100% late in the accumulating season, their value for SWE estimation lies mainly in the ability to indicate the timing and rate of snow cover disappearance in the melting season. The fSCA measurement cannot directly indicate the absolute amount of SWE or snow depth, making it primarily useful for generating retrospective data. Incorporating sub-kilometer snow products with a stronger instantaneous correlation with SWE would potentially better enable near real-time assessment of snow-water resource changes.

New techniques are being developed to retrieve changes in SWE or snow depth from synthetic aperture radar (SAR) and laser altimeter (Guneriussen et al., 2001; Leinss et al., 2015; Lievens et al., 2019; Besso et al., 2024; Oveisgharan et al., 2024; Hoppinen et al., 2024; Shrestha and Barros, 2025; Oveisgharan et al., 2025). In the Kelan watershed, interferometric SAR

https://doi.org/10.5194/egusphere-2026-5345
Preprint. Discussion started: 23 September 2026

(InSAR), depolarization ratio, and lidar-based approaches have been investigated to generate snow products. Hu et al. (2022) generated snow depth from ICESat-2 in flat regions with an R^2 of up to 0.88 compared against 16 in situ measurements, while identifying challenges in estimating snow depth over mountainous regions and vegetation-covered areas. Xiong et al. (2025) found that the snow depth retrieved directly from Sentinel-1 C-band backscatter polarization ratios was not consistent with in situ measurements. Within Altay, backscatter polarization ratios varied among areas of comparable snow depth potentially linked to differences in surface roughness. They discovered that a rough snow/soil interface tends to increase backscatter cross-polarization, and thus bias correction for surface roughness is needed before retrieving snow depth from C-band backscatter polarization ratio. Zhou et al. (2025) applied the InSAR approach to retrieve 12-day swath-based ΔSWE from Sentinel-1 C-band for the snow season during years 2019-2021. The reported root mean square error of ΔSWE was ~ 9.54 mm for dry snow in two snow seasons, providing a valuable dataset in this region. ΔSWE is retrieved from measured phase changes, which are limited to a 2π phase cycle. The retrieval process involves phase unwrapping algorithms, producing potential errors in the retrieved ΔSWE (Hoppinen et al., 2024; Margulis et al., 2026; Oveisgharan et al., 2024). Apart from the spatiotemporal discontinuities in spaceborne snow retrievals, the value of assimilation of new remotely sensed snow products needs to be investigated.

This work uses a previously developed snow reanalysis framework to generate a space-time continuous daily SWE dataset at 150-m resolution over Water Years (WYs, Oct. 1st, 2018 to September 30th, 2025) by assimilating retrieved HLS fSCA using a Particle Batch Smoother (PBS) approach (Margulis et al., 2015, 2019). The snow reanalysis dataset is used as a baseline to 1) quantify the snow water storage and its distribution in the Kelan watershed in Altay, 2) characterize the likelihood and spatial patterns of residual phase wrapping issues in InSAR derived ΔSWE, and 3) assess the value of InSAR-derived ΔSWE from Sentinel-1 (WYs 2020 and 2021) and LuTan-1 satellites (WY 2024) for constraining modeled SWE estimates.

2. Study area, Datasets, and Methodology

2.1 Study area

The study area, the Kelan River basin (N87-88, W47-48), is located in Altay Prefecture, northern Xinjiang, China (Fig. 1). It is part of the Altay Mountains, bounded by four countries. Similar to the American Cordillera, westerly winds are predominant over the Altay Mountains (Zhang et al., 2018). The continental climate features cold and wet winters followed by warm and dry summers (Aizen et al., 2006; Yang et al., 2019). A significant portion of fresh water in the Altay prefecture is from Altay Mountain snowmelt. In situ sites are sparsely distributed and typically not publicly accessible. In the Kelan River basin, a meteorological station (Altay Meteo.) is publicly available and has been established since the early 1950s. The average elevation is ~1320 m in the Kelan watershed, ranging from ~ 500 m to 3200 m (Fig. 1). The forest cover (FC) fraction computed from the Global Land Cover Facility (GLCF) dataset is ~ 1.48 % on average, mostly located in areas at low to middle (< 1500 m) elevations. Based on the in situ meteorological site, the long-term averaged annual precipitation at Altay is ~ 240 mm. The average temperature ranges from ~ -20 °C in winter to ~ 20 °C in summer. A significant increasing trend (~ 2.4˚C) in the

https://doi.org/10.5194/egusphere-2026-5345
Preprint. Discussion started: 23 September 2026

December to February average air temperature is observed over the past 70 years, consistent with previous findings in Zhang et al. (2018).

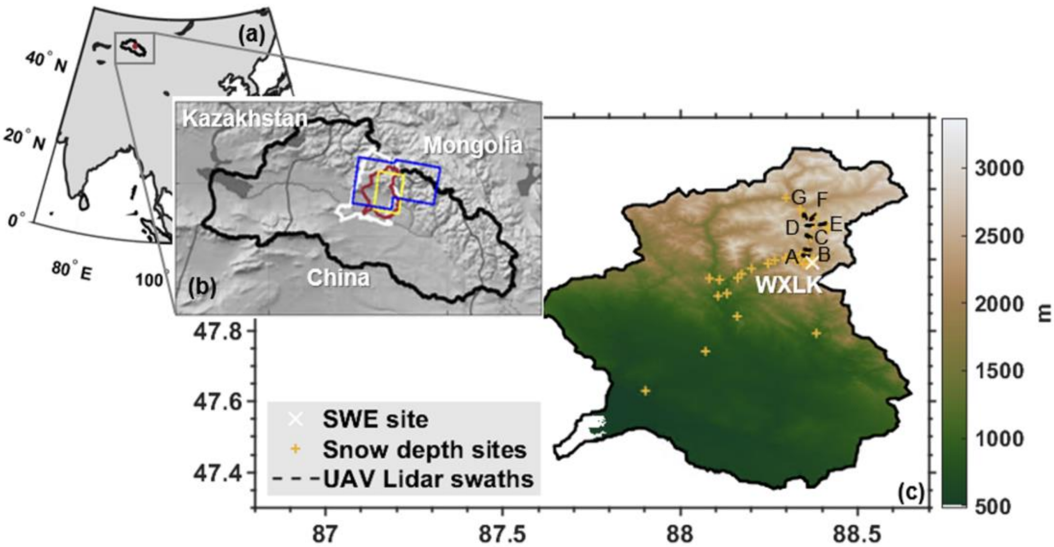

Figure 1: Panel (a) shows the relative location of the Irtysh River basin (black boundary) in Asia. Panel (b) shows the Altay prefecture (white boundary) and the Kelan sub-watershed (red boundary) within the Irtysh River basin. The blue and yellow boxes show the Sentinel-1 and LuTan-1 measurement boundaries, respectively. Panel (c) shows the elevation distribution, in situ SWE and snow depth sites, and UAV Lidar snow depth swaths (A-G) at the Kelan watershed.

2.2 Datasets and methodology

2.2.1 In situ sites and Lidar measurements

The Kelan watershed only contains one in situ SWE site, the WuXiLike (WXLK) site. Daily SWE observations measured by snow pillow are available in WYs 2020, 2021, and 2024 in this study. The WXLK site is located in a flat, mid-elevation area (~2146 m), with forest coverage of ~3.72%. In addition to the SWE site, snow-depth measured by an ultrasonic sensor or a camera installed manually are available over WYs 2020 to 2025 at 40 sites, most of which have only one or two years of record. The most sites operating in a single year is in WY 2025, with snow depth measurements at 33 sites. The in situ snow depth sites are located at elevations ranging from 600 m to 2700 m, with forest cover of up to 16% and slope of up to 30°.

Seven Uncrewed Aerial Vehicle (UAV) Lidar snow depth swaths collected on 7 January 2025 are used for verification of snow depth spatial distribution. The UAV Lidar measurements are narrow swaths approximately 1 km by 5 km with a raw spatial resolution of ~ 0.5 m. They are aggregated to the ~150 m model resolution for comparison with the prior and posterior snow reanalysis snow depth estimates.

https://doi.org/10.5194/egusphere-2026-5345
Preprint. Discussion started: 23 September 2026

2.2.2 Fractional snow covered area

The Harmonized Landsat and Sentinel (HLS) version 2.0 collection (Claverie et al., 2018) is used to generate fractional snow covered area (fSCA) as measurement inputs. The harmonization of Landsat and Sentinel products involves the following processes: 1) atmospheric correction, 2) cloud and cloud shadow masking, 3) normalization to a nadir-view geometry, 4) spectral bandpass adjustment, 5) spatial standardization to a common 30 m × 30 m Military Grid Reference System (MGRS) grid through harmonized gridding and projection, and 6) data and metadata formatting. As shown in Table S1 in the Supplement, the HLS datasets include surface reflectance measured from the Operational Land Imager (OLI) on Landsat 8 (since April 2013), Landsat 9 (since October 2021), and the Multi-Spectral Instrument (MSI) on Sentinel-2A (since November 2015), and Sentinel-2B (since July 2017). Individual Landsat and Sentinel-2 satellites have temporal resolutions of 16 days and 10 days, respectively.

Reflectivity at tiles 45UXP, 45UWP, 45TWN, and 45TXN covering the Kelan watershed was used in this study. This work only adopted images with cloud cover less than 40% (Liu et al., 2021; Fang et al., 2022). Pixels defined as water or cloud, determined from the quality control files, are screened out. The number of images available was limited before 2018, when only two satellites were in orbit. Since 2018, the average number of available images (January to September) for data assimilation after screening ranges from ~ 15 to 36 per year. Therefore, this work generates snow reanalysis data beginning in WY 2018.

The Snow Property Inversion from Remote Sensing (SPIReS, Bair et al., 2021) approach is selected to retrieve fSCA by minimizing the residual of the unmixing spectral equation:

$$R_\lambda = \varepsilon_\lambda + f_{sca} r_{sca,\lambda} + f_{shade} r_{shade,\lambda} + f_{ice} r_{ice,\lambda} + f_{canopy} r_{canopy,\lambda} \tag{1}$$

where f and r_λ are the fractional covered area and reflectance of each end member, namely snow (f_{sca}), shade (f_{shade}), ice (f_{ice}) and canopy (f_{canopy}). The fractional covered areas of the four end members sum to 1. ε_λ is the residual error at each wavelength λ that needs to be minimized. R_λ is the total reflectance provided in the downloaded data.

Ice and canopy are treated as constant background information. The total reflectance $R_{0,\lambda}$ in summertime, when snow is absent is assumed to be the summed reflectance. $r_{sca,\lambda}$ can be interpolated from a pre-computed lookup table (LUT), given snow grain radius (r_g), dust concentration (δ), illumination angle (cosZ), and wavelength (λ) as four inputs. $r_{shade,\lambda}$ is set to be 0 in Bair et al. (2021) following the ideal black surface assumption in Smith et al. (1990). Under these assumptions, Eq. (1) is simplified to include four unknowns, namely, f_{sca}, r_g, δ, and f_{shade}:

$$\varepsilon_\lambda = R_\lambda - \boldsymbol{f_{sca}} F\left(\boldsymbol{r_g}, \boldsymbol{\delta}, \cos Z, \lambda\right) - (1 - \boldsymbol{f_{sca}} - \boldsymbol{f_{shade}}) R_{0,\lambda} \tag{2}$$

The bands labeled Coastal Aerosol, Blue, Green, Red, Near Infrared (NIR) Narrow, Short-Wave Infrared (SWIR) 1, and SWIR 2 are used to form seven equations in terms of the four unknowns. Eq. (2) was solved by minimizing the residual ε_λ, using sequential of quadratic programming under the constraint that the fractions of the four end members sum to one. Additionally, f_{sca} and f_{shade} should be positive numbers less than one.

https://doi.org/10.5194/egusphere-2026-5345
Preprint. Discussion started: 23 September 2026

The static inputs to the SPIReS method used in the work include canopy cover from GFCC (Sexton et al., 2013; Townshend, 2016) in the year 2015, the digital elevation model from SRTM (Farr et al., 2007; NASA JPL., 2013), and the fraction of ice from RGI (RGI Consortium, 2023). Dynamic inputs include snow-free and snow-on reflectance from HLS. Clouds and water bodies are determined from the HLS quality control files.

2.2.3 Other input datasets

Forcings, DEM, land cover, and forest cover datasets used in this work remain the same as those used in the WUS snow reanalysis dataset (Fang et al., 2022). In summary, the 1 arcsecond SRTM DEM is aggregated, 1 km AVHRR (Hansen et al., 2000; U.S. Geological Survey, 2017) landcover dataset is downscaled, and 30-m GFCC forest cover dataset is aggregated to the ~ 150 m model resolution, balancing both accuracy and computational cost of the snow reanalysis data (Figure S1, S2). The MERRA2 forcing dataset (Gelaro et al., 2017; Global Modeling and Assimilation Office (GMAO), 2015a, b, c) is downscaled and bias corrected following the methods introduced in Margulis et al. (2019) and Liu & Margulis (2019). The uncertainties of air temperature and dew point temperature were quantified using the in situ meteorological dataset at the Altay meteorological station from WYs 1985 to 2025. The uncertainty parameters are summarized in Table S2.

2.2.4 Snow Reanalysis framework

This work adopted the snow reanalysis framework (Margulis et al., 2015, 2019) previously developed and successfully applied to generate long-term space-time continuous SWE in the Sierra Nevada (Margulis et al., 2016), over the Western U.S. (WUS, Fang et al., 2022), the Andes (Cortés and Margulis, 2017), and the High Mountain Asia (HMA, Liu et al., 2021). The datasets have been verified against independent observations. In short, the snow reanalysis framework consists of a forward land surface model (LSM) and a data assimilation process. In the forward modeling step, the SSiB-SAST LSM (Sun and Xue 2001) with three-layer snowpack is used. The Liston (2004) subpixel snow cover depletion model is coupled in the LSM to link SWE and fractional snow covered area (fSCA) controlled by a statistical parameter, Coefficient of Variation (β in Table S2). Meteorological forcings are bias corrected and perturbed to drive the LSM for generating prior ensembles. In this work, the number of ensemble members is set to 100, with each member assigned an equal prior weight of 0.01. The particle batch smoother (Margulis et al., 2015) is used to update the weights of ensembles assuming the difference between observed and estimated states follows a zero-mean multivariate Gaussian distribution with a specified error covariance matrix. This approach updates all modeled states, such as SWE and snow depth, at the end of each water year using all qualified measurements from that year. Median and interquartile range of prior and posterior SWE values are extracted based on the ensembles and their prior and updated weights, respectively.

In this work, the same framework is adopted to generate constrained baseline snow reanalysis SWE estimates. For the baseline run, the selected observations used to constrain modeled states are the new fSCA retrievals from seamless HLS surface reflectance as described in Sect. 2.2.2. The same measurement errors of 10% (Fang et al., 2022) are set to both Landsat and Sentinel retrievals. We further evaluate the effect of assimilating InSAR ΔSWE retrieval at the pixel level using the same

https://doi.org/10.5194/egusphere-2026-5345
Preprint. Discussion started: 23 September 2026

approach in the experiment run. A total of 2000 pixels located at elevations above 1250 m are randomly selected. Measurement errors are set to 10 mm for InSAR ΔSWE retrievals as discussed in Sect. 2.2.6.

2.2.5 Snow metrics and evaluation statistics

In this work, we computed peak SWE in depth units, peak SWE volume, snow start days, snow melt-out days, and snow cover duration from daily SWE. Melt-out day is defined as the first day when SWE is below 5 mm or the corresponding SWE volumes over a defined spatial area after the peak. Evaluation statistics includes correlation coefficients (r), mean difference (MD), unbiased root mean square difference (uRMSD). Temporal statistics are computed for daily SWE and snow depth over October to June.In this work, we computed peak SWE in depth units, peak SWE volume, snow start days, snow melt-out dates, and snow cover duration from daily SWE. Melt-out day is defined as the first day when SWE is below 5 mm or the corresponding SWE volumes over a defined spatial area after the peak. Evaluation statistics, including includes correlation coefficients (r), mean difference (MD), and unbiased root mean square difference (uRMSD) were computed. Temporal statistics are computed for daily SWE and snow depth over October to June. Note that comparisons between data at a ~ 150 m grid scale and in situ measurement at point scale are subject to spatial representativeness issues, as the gridded data characterize conditions averaged over an area, whereas in situ measurements represent conditions at a specific location. Consequently, the differences between the two datasets may reflect both actual data errors and subgrid-scale spatial variability. Therefore, uRMSD is used to evaluate the variability and agreement between the datasets while minimizing the influence of systematic bias. This is particularly important in mountainous areas, where topography can vary substantially within a 150 m spatial resolution. Improved statistic relative to in situ measurements indicate that the generated data are more consistent with the point measurements. Degraded statistics, on the other hand, suggest discrepancies between the generated data and in situ measurements, which may be caused by factors such as topography variability, snow drift, and forest cover. Similar to (Fang et al. (2022), the snow-reanalysis grid cell with the lowest uRMSD among the nine grid cells nearest to the in situ site is selected for comparison.

2.2.6 InSAR retrieved ΔSWE and $\Delta\phi$ products

Recently, new snow products retrieved from Sentinel-1 using the InSAR technique were developed in the Altay domain. Zhou et al. (2025) generated the 12-day InSAR retrieved ΔSWE from Sentinel-1 with a spatial resolution of ~75 m × 75 m over WYs 2020-2021. The raw Sentinel-1 SLC data were processed by 1) co-registering and phase-unwrapping by the ISCE2 stack processor, 2) correcting errors from the troposphere, topography, and phase unwrapping using MintPy (Zhang, Fattahi, and Amelung 2019; https://github.com/insarlab/MintPy), and 3) calibrating $\Delta\phi$ using in situ measurements, and 4) converting the corrected $\Delta\phi$ to ΔSWE. Additionally, 4-day InSAR retrieved ΔSWE and coherence were generated from the LuTan-1 L-band mission using a similar approach. Based on experiments, for microwave signals with low frequencies (< 16 GHz), volume scattering can be neglected for a homogeneous dry snowpack (Leinss et al., 2015). Under this assumption, InSAR-retrieved phase change is related to snow depth changes via Guneriussen et al. (2001):

https://doi.org/10.5194/egusphere-2026-5345
Preprint. Discussion started: 23 September 2026

$$\Delta\phi = -2k\left[\mathrm{SD}_{t2}\left(cos\theta - \sqrt{\varepsilon_{t2} - sin\theta^2}\right) - \mathrm{SD}_{t1}\left(cos\theta - \sqrt{\varepsilon_{t1} - sin\theta^2}\right)\right] \quad (3)$$

where $\Delta\phi$ is the change of phase due to snow changes, SD is the snow depth at t1 and t2, θ is the incidence angle in radians, k is the wave number (2π/λ), λ is the free-space wavelength (0.055 m for Sentinel-1 C-band sensor, and 0.24 m for LuTan-1 L-band sensor), and ε is the snow permittivity. Assuming snow density does not change yields a simplified equation:

$$\Delta\phi = -2k\Delta\mathrm{SD}\left(cos\theta - \sqrt{\varepsilon - sin\theta^2}\right) \quad (4)$$

For dry snow, ε can be estimated by (Matzler, 1996; Wiesmann and Mätzler, 1999):

$$\varepsilon = 1 + 1.6 \times 10^{-3}\rho_s + 1.8 \times 10^{-9}\rho_s^3 \quad (5)$$

where ρ_s is snow density in kg/m^3.

Leinss et al. (2015) found $cos\theta - \sqrt{\varepsilon - sin\theta^2}$ is approximately equal to $-\frac{\alpha}{2}\left(1.59 + \theta^{\frac{5}{2}}\right)\frac{\rho_s}{\rho_w}$, where ρ_s is snow density and ρ_w is water density. Based on this simplification, a linear relationship between $\Delta\phi$ and ΔSWE can be derived from Eq. (3) and (4):

$$\Delta\phi = 2k\frac{\alpha}{2}(1.59 + \theta^{\frac{5}{2}})\Delta\mathrm{SWE} \quad (6)$$

where α is a correction factor and is set to 1 in Sentinel and LuTan InSAR ΔSWE retrieval. For dry snow with a snow density less than 400 kg/m^3, and an incidence angle of less than 50˚, the uncertainty of ε is less than 10% for $\alpha = 1$. $\Delta\phi$ computed from Eq. (3), (4) and (6) are unwrapped. In contrast, due to its nature, measured $\Delta\phi$ is confined to a range of 2π, where the phase can be wrapped for wavelength-dependent critical values of ΔSWE corresponding to ~0.02-0.03 m for C band and 0.08 – 0.14 m for L band. In cases where ΔSWE exceeds these critical values, phase wrapping/unwrapping needs to be carefully solved (Margulis et al., 2026).

The computation of $\Delta\phi$ from Eq. (4) can be erroneous during snow compaction season, where snow density cannot be assumed to be constant. Equations (3) and (6) are both valid during snow compaction season and are thus used in this work.

The reported RMSE of Sentinel-1 C-band retrieved ΔSWE from is ~ 9.54 mm (Zhou et al. 2025, ~1/3 of the critical ΔSWE). Thus, the measurement error of ΔSWE is set to be 10 mm for Sentinel-1 ΔSWE retrievals. The same measurement error is set to L-band ΔSWE retrievals considering a shorter repeat cycle yet longer wavelength.

The InSAR retrieved data (~ 100 m) were interpolated to the snow reanalysis grid (~150 m). In WY 2020 and WY 2021, ΔSWE generated from Sentinel-1 C-band measurements covers the whole accumulation seasons for every 12 days (Table 1). In WY 2024, LuTan-1 L-band measurements were used to generate ΔSWE for every 4 days from January 12th to February 9th, 2024. The unused interferometric pairs in those years were marked as low quality or low coherence due to heavy snowfall or wet snow. Figure 1 (b) displays the measurement boundaries of the Sentinel-1 satellite (blue box), covering most of the study area, and the LuTan-1 satellite (yellow box), partially covering the eastern part of the study area. The averaged local incident angles within the Kelan watershed are ~43˚ and 39˚ for Sentinel-1 and LuTan-1 satellites, respectively (Fig. S3). At the WXLK site, the incident angle is 45.5˚ from the Sentinel-1 satellite and 33.4˚ from the LuTan-1 satellite.

https://doi.org/10.5194/egusphere-2026-5345
Preprint. Discussion started: 23 September 2026

Table 1. Periods with available ΔSWE data

Index	WY 2020 (Sentinel-1)	WY 2021 (Sentinel-1)	WY 2024 (LuTan-1)
1	11 Oct 2019 - 23 Oct 2019	11 Sep 2020 - 23 Sep 2020	12 Jan 2024 - 16 Jan 2024
2	23 Oct 2019 - 04 Nov 2019	23 Sep 2020 - 05 Oct 2020	16 Jan 2024 - 20 Jan 2024
3	04 Nov 2019 - 16 Nov 2019	05 Oct 2020 - 17 Oct 2020	20 Jan 2024 - 24 Jan 2024
4	16 Nov 2019 - 28 Nov 2019	17 Oct 2020 - 29 Oct 2020	24 Jan 2024 - 28 Jan 2024
5	28 Nov 2019 - 10 Dec 2019	29 Oct 2020 - 10 Nov 2020	28 Jan 2024 - 01 Feb 2024
6	10 Dec 2019 - 22 Dec 2019	10 Nov 2020 - 22 Nov 2020	01 Feb 2024 - 05 Feb 2024
7	22 Dec 2019 - 03 Jan 2020	22 Nov 2020 - 04 Dec 2020	05 Feb 2024 - 09 Feb 2024
8	03 Jan 2020 - 15 Jan 2020	04 Dec 2020 - 16 Dec 2020	
9	15 Jan 2020 - 27 Jan 2020	16 Dec 2020 - 28 Dec 2020	
10	27 Jan 2020 - 08 Feb 2020	28 Dec 2020 - 09 Jan 2021	
11	08 Feb 2020 - 20 Feb 2020	09 Jan 2021 - 21 Jan 2021	
12	20 Feb 2020 - 03 Mar 2020	21 Jan 2021 - 02 Feb 2021	
13	03 Mar 2020 - 15 Mar 2020	02 Feb 2021 - 14 Feb 2021	
14	15 Mar 2020 - 27 Mar 2020	14 Feb 2021 - 26 Feb 2021	
15	27 Mar 2020 - 08 Apr 2020	26 Feb 2021 - 10 Mar 2021	
16		10 Mar 2021 - 22 Mar 2021	
17		22 Mar 2021 - 03 Apr 2021	

3. Results and Discussion

3.1 Verification of results against in situ and Lidar data

The time series of reanalysis SWE and snow depth estimates are verified against in situ measurements. At the WXLK site as shown in Fig. 2, after assimilation of HLS fSCA, posterior SWE and snow depth improved from the prior with lower uRMSD and uncertainties for all three WYs (i.e., WY 2020, 2021, 2024). The reanalysis SWE estimates capture the pattern of the in situ SWE time series, with correlation coefficients above 0.9 for both prior SWE and posterior SWE compared with in situ SWE. Based on the in situ data, approximately 25 mm of SWE is observed on 25 September 2020, as a result of a snowstorm with over 30 mm of snowfall. In contrast, only 7 mm of SWE is estimated by posterior data on the same day. For this specific case, posterior air temperature on 24 September 2020, is potentially so high that a large portion of storm fall as rainfall. Approximately 3 cm of SWE is carried over into October base on the in situ site in contrast to a 1 cm of posterior SWE at the end of September 2020. The current WY period runs from 1 October of previous year to 30 September of the current year. Thus, snow in September 2020 is constrained by fSCA in January to May of this year, introducing potential error due to interannual variability. For the Kelan watershed, 1 September is recommended to be set as the beginning of the WY to better capture snow accumulation in early winter. Mechanisms to model early-season snow events in the land surface model

https://doi.org/10.5194/egusphere-2026-5345
Preprint. Discussion started: 23 September 2026

need to be carefully reviewed and enhanced in the future. As illustrated in Fig 2 (d-f), the uRMSD of daily SWE is reduced from 0.041 m (16% of in situ peak SWE) to 0.025 m (10% of peak in situ SWE), 0.050 m (14% of in situ peak SWE) to 0.031 m (9% of in situ peak SWE), and 0.120 m (30% of in situ peak SWE) to 0.051 m (13% of in situ peak SWE) from the prior to the posterior in WY 2020, 2021, and 2024, respectively. In situ snow depth measurements obtained by camera are used for verification. Similar performance is observed for snow depth at the WXLK site (Fig 2 g-i). Based on snow depth, the posterior melt-out dates are within a week, whereas the prior estimates tend to melt out over 1-2 weeks later than the in situ measurements. Posterior SWE and snow depth in WY 2024 are significantly improved from the overestimated prior, illustrating the robustness of the retrieved HLS fSCA in updating SWE using the current snow reanalysis framework with biased forcing inputs.

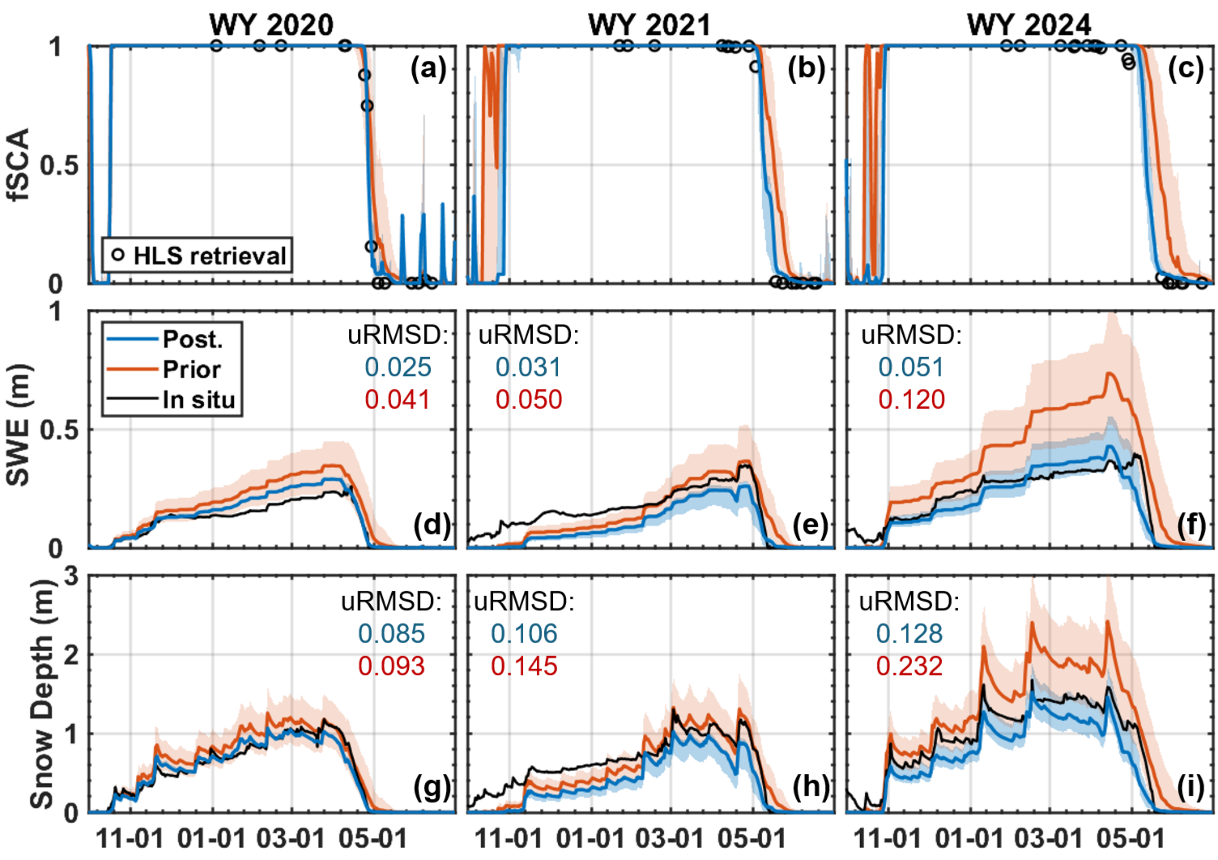

Figure 2: Panels (a) to (c) show prior (solid red lines, open loop) and their inter-quartile range (IQR, red shades), posterior (solid blue lines, after data assimilation) and their IQR (blue shade), and retrieved HLS fSCA (black circles) at the WXLK site over WY 2020, 2021, and 2024. Panels (d) to (f) show prior, posterior, and in situ (black lines) SWE over three years. Panels (g) to (i) show prior, posterior, and in situ snow depth over three years.

https://doi.org/10.5194/egusphere-2026-5345
Preprint. Discussion started: 23 September 2026

The reanalysis snow depth estimates are additionally verified against in situ snow depth measurements. Except for the WXLK site, for sites located at elevations above 1000 m, only the DaDongGou (DDG) site contains over 2 years of daily snow depth estimates. Figure 3a shows that at the DDG site, snow reanalysis dataset fairly captures the in situ snow depth measurements in WYs 2020, 2021, and 2025 with uRMSD of 0.050 m, 0.038 m, and 0.094 m, respectively. All are significantly improved by over 30% from the prior. This site is located in a flat area of a valley surrounded by mountains (Fig. 2g DaDongGou in Zhou et al. 2025). In WY 2025, the 33-site average relative uRMSD percentage is ~9 % of the peak snow depth and relative MD percentage is ~ 3 %. The site on the rocky hill (Fig. 3e) has a high relative MD of ~ 19 %, potentially caused by a high MD relative to a low in situ peak snow depth. There are three sites under the canopy that are close to each other, with distances of less than 500 m. However, the in situ peak snow depth estimates varied among 1.40 m, 1.62 m and 2.42 m, illustrating heterogeneity of snow depth distribution. The posterior snow depth distribution fairly characterizes two out of three sites under canopy. Posterior snow depth at site #3 was underestimated with a relative MD of 23 %. After bias removal, the posterior relative uRMSD at this site is reduced to 12.31 %. The verification of snow depth measurements at nearby sites shows that assimilation of fSCA measurements can capture the sub-canopy snow depth. Potential sources of uncertainty include the assumption of a temporally constant canopy fraction in the fSCA retrieval algorithm and the inherent limitations of the land surface model itself.

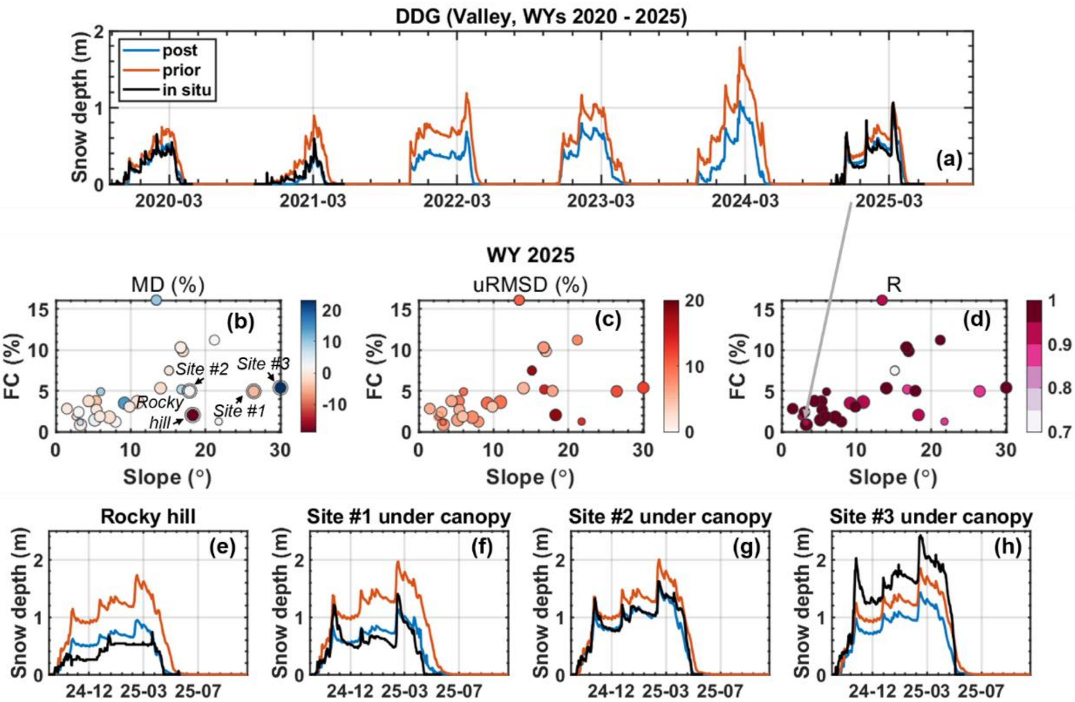

Figure 3: Panel (a) shows the prior (red), posterior (blue), and in situ (black) daily snow depth timeseries at the DDG sites. Panels (b) to (d) show the distribution of MD in percentage (in situ - posterior) normalized by in situ peak snow depth of each site, uRMSD in percentage and R over forest coverage and slope. The sizes of scatters are proportional to the elevation. Panel (e) to (h) show the time series of daily snow depth over Rocky hill and three nearby sites under canopy.

https://doi.org/10.5194/egusphere-2026-5345
Preprint. Discussion started: 23 September 2026

The comparison of point-scale in situ measurements against grid estimates is subject to spatial representativeness issues. The snow reanalysis snow depth is further compared against the UAV Lidar snow depth measurements. Figure 4 shows that the spatial distribution of posterior snow is consistent with the raw Lidar snow depth, with deeper snow located in the northwestern part of the swath. The magnitude and spread of snow depth values in the posterior snow reanalysis data are comparable to both raw and aggregated Lidar snow depth (Fig. 5a, Path A). In contrast, prior snow depth is uniformly distributed over the swath path (Fig. 4d), yielding a mean overestimation of 0.31 m (Fig. 5d). Among all 7 swaths, the posterior snow depth has higher correlation compared against the aggregated Lidar data, with most having a lower absolute MD (mean of -0.120 m) than the prior (mean MD of -0.294 m). The comparable uRMSD between prior and posterior snow depth suggests that both estimates have similar residual standard deviation after bias removal. The ranges of posterior snow depth values are closer to the raw Lidar data than those of the prior, whereas prior snow depth tends to be deeper on average with a narrow spread. Overall, posterior estimates reasonably reflect the magnitude and spatial pattern of snow depth distribution over the UAV swaths.

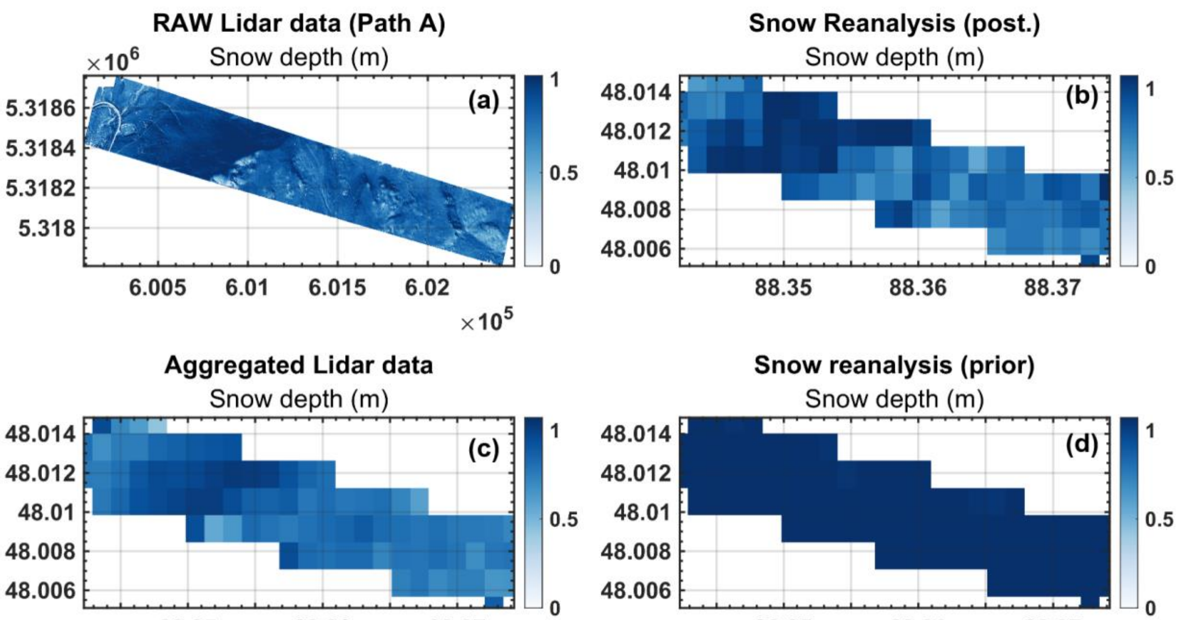

Figure 4: Spatial distribution of snow depth in (a) raw LiDAR data with spatial resolution at ~ 0.5 m, (b) aggregated LiDAR data at ~ 150 m, (c) posterior snow reanalysis at ~ 150 m, (d) prior snow reanalysis at ~ 150 m.

https://doi.org/10.5194/egusphere-2026-5345
Preprint. Discussion started: 23 September 2026

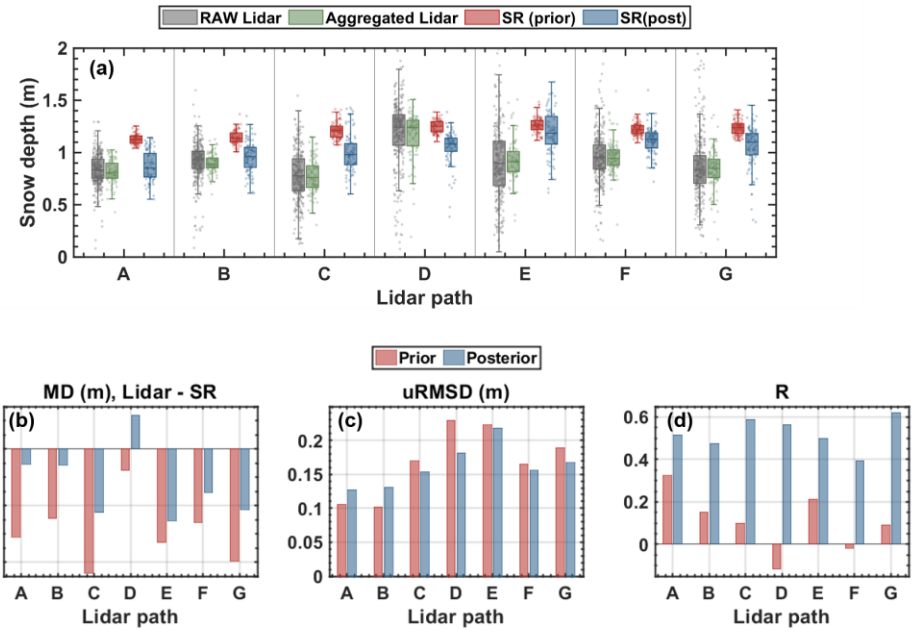

Figure 5: Panel (a) shows the box plot of raw lidar (gray), aggregated lidar (green), prior snow reanalysis (red), and posterior snow reanalysis (blue) snow depth distribution over seven UAV Lidar swath. For each swath, the correlation R, uRMSD and MD of prior and posterior snow depth over aggregated Lidar snow depth, is shown in panel (b) to panel (d), respectively.

3.2 Space-time distribution of Altay SWE from the baseline snow reanalysis data

Over WYs 2018-2025, the 8-year average total peak SWE volume is ~0.76 km^3, with the highest total SWE volume of 1.16 km^3 in WY 2024 and the lowest peak SWE volume of 0.56 km^3 in WY 2021. The average day of peak total SWE volume is DOWY 166 (~15 March; Fig. 6d dashed lines). A pronounced snowfall event is likely to occur in March. The late snowfall caused either an increase in SWE volumes during the melting season (WY 2019, 2021, 2023, 2024) or a new peak of SWE (WY 2022 and 2025). SWE melted out in mid-June in WYs 2020 to 2022, and WY 2025, whereas it melted out late in mid-August in WY 2023 and 2024 due to higher SWE volumes and late snowfall events. The sensitivity of SWE volume estimates to the assimilation of different fSCA products including Landsat 8/9 alone, Sentinel-2, and harmonized Landsat and Sentinel measurements is discussed in Text S1 and Fig. S4. Assimilation of fSCA observations from two satellites produces SWE volumes comparable to those obtained by assimilating fSCA from all HLS products, illustrating that ~ 10+ effective fSCA images in the melting season per year for each pixel can reasonably constrain SWE volume estimates.

https://doi.org/10.5194/egusphere-2026-5345
Preprint. Discussion started: 23 September 2026

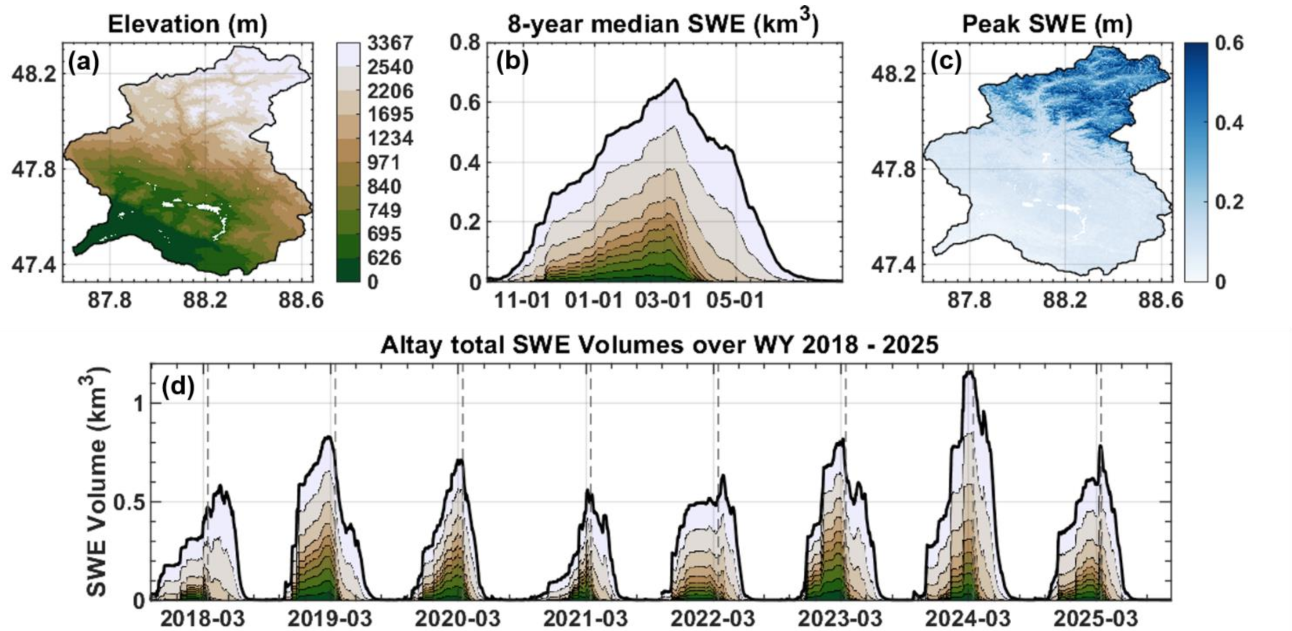

Figure 6: Spatial maps of elevational bands (a), elevational distribution of 8-year median daily SWE volumes timeseries over WYs 2018 to 2025 (b), and pixel-wise peak SWE (c) in meters. Panels (d) is the elevational distribution of daily SWE volumes at the Kelan watershed for each year. In the stacked area plots (b and d), each colored segment represents SWE volumes from the specific elevational bands shown in panel (a). The bold black line shows total SWE volume. The dashed vertical line represents the average peak SWE day on March 15th.

SWE timing and volumes vary significantly across different elevational bands. Shaded colors in Fig. 6 (b) and (d) represent the amount of daily SWE across 10 elevational bins, each of which contains a similar geographical area of ~ 515 km^2. Figure 7 illustrates that, on average, over 35 % of snow is stored above ~1500 m. Approximately one-quarter of snow water is stored in the highest elevation band (> ~2500 m) of the watershed, with limited availability of in situ sites. Snow water volume and melt-out time exhibit a heterogeneous spatial distribution. For example, WY 2018 is the driest year for areas with elevations lower than 1500 m. In contrast, it is the second wettest year over 8 years above 1500 m, where more than 80 % of water is distributed in this year. The average number of snow-on days is around 160 over the record at the Kelan watershed. At higher elevations, the 8-year average number of snow-on days can be as high as 240, more than 3 months longer than areas located lower than ~1500 m. Lower elevations exhibit a more pronounced increase in snow cover duration from wet years to dry years than higher elevations. The differences in peak SWE days between high elevation bins and low elevation bins are around ~ 1 to 2 months. SWE at elevations lower than 1680 m tends to melt out in early April. In contrast, SWE at higher elevations melted out ~ 2 months later than the low elevation on average.

https://doi.org/10.5194/egusphere-2026-5345
Preprint. Discussion started: 23 September 2026

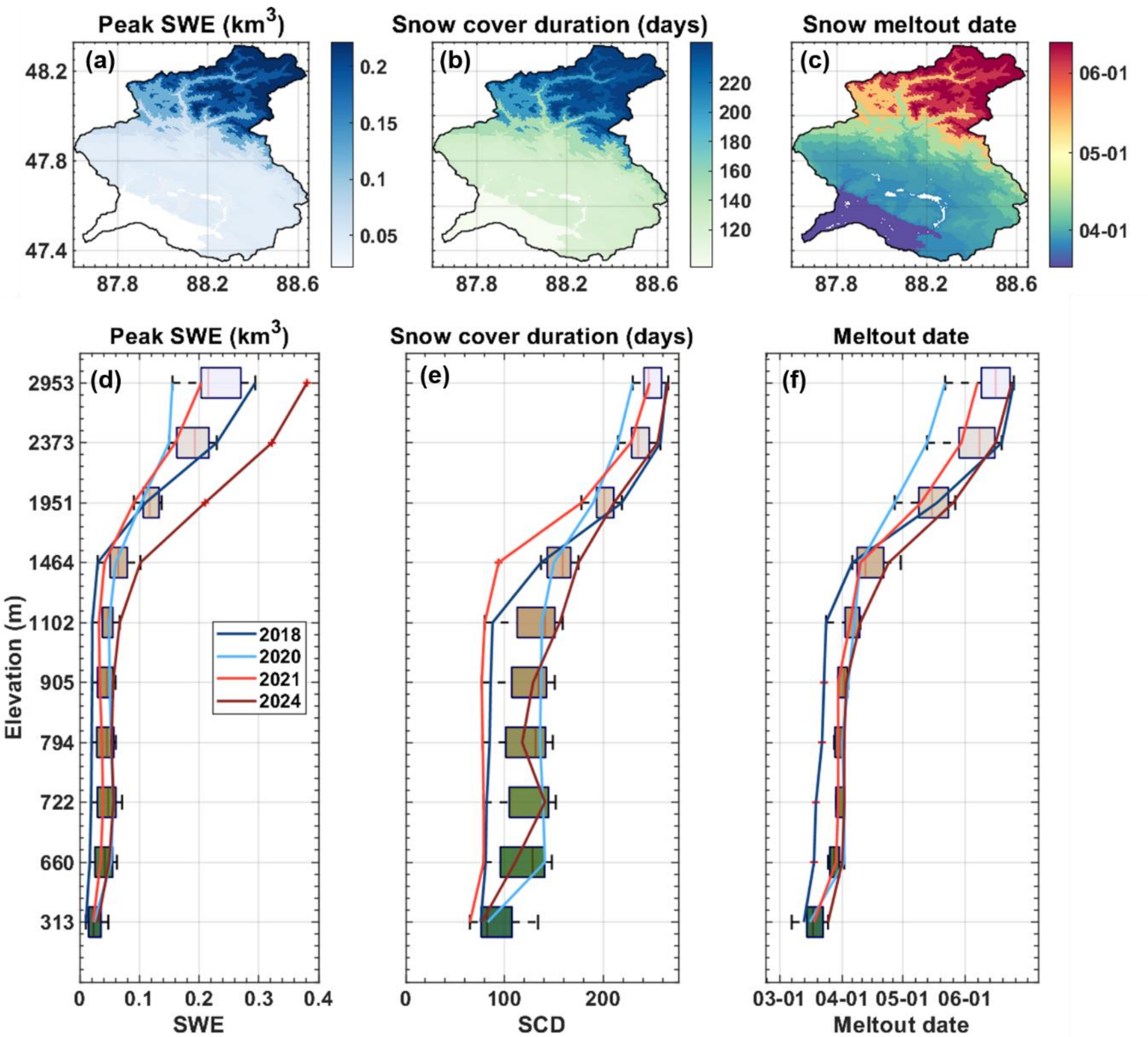

Figure 7: Spatial distribution (top panels) and boxplots (bottom panels) of 8-year averaged peak SWE volumes (a and d), snow cover duration (b and e) and snow meltout dates (c and f) over each elevational bin.

3.3 The likelihood of phase wrapping issue based on the snow reanalysis data

This section uses snow reanalysis dataset to estimate the likelihood of wrapped phase, a key source of uncertainty in InSAR retrievals. Recall that the critical ΔSWE values are ~0.02-0.03 m in C-band and 0.08-0.14 m in L-band for incidence angles from 10˚ to 60˚, corresponding to a 2π phase wrapping cycle using Eq. (6). Figure 8 (a) to (h) illustrate that SWE changes by more than 0.02 m over 12 days in ~20% of the pixel-time samples before the averaged peak day (day of water year 166) in most of the years in the Kelan watershed. For wet years such as WYs 2023 and 2024, as much as ~28% of the watershed exhibits ΔSWE >0.02 m over 12 days, likely to be affected by phase wrapping in the C-band InSAR retrievals. In contrast,

https://doi.org/10.5194/egusphere-2026-5345
Preprint. Discussion started: 23 September 2026

fewer than 2% of pixel-time samples exhibit 12-day ΔSWE greater than 0.08 m, indicating a substantially lower likelihood of phase wrapping for L-band observations and supporting their use for SWE retrieval in the Kelan watershed. Figure 6i shows that the average proportion of pixel-time with ΔSWE >0.02 m is reduced from 20% to 4% when the frequency of satellite measurements increases from 12 days per measurement to 3 days. Despite the longer revisit interval, the 12-day L-band
360 measurement pairs are less prone to phase wrapping than 3-day C-band measurement pairs.

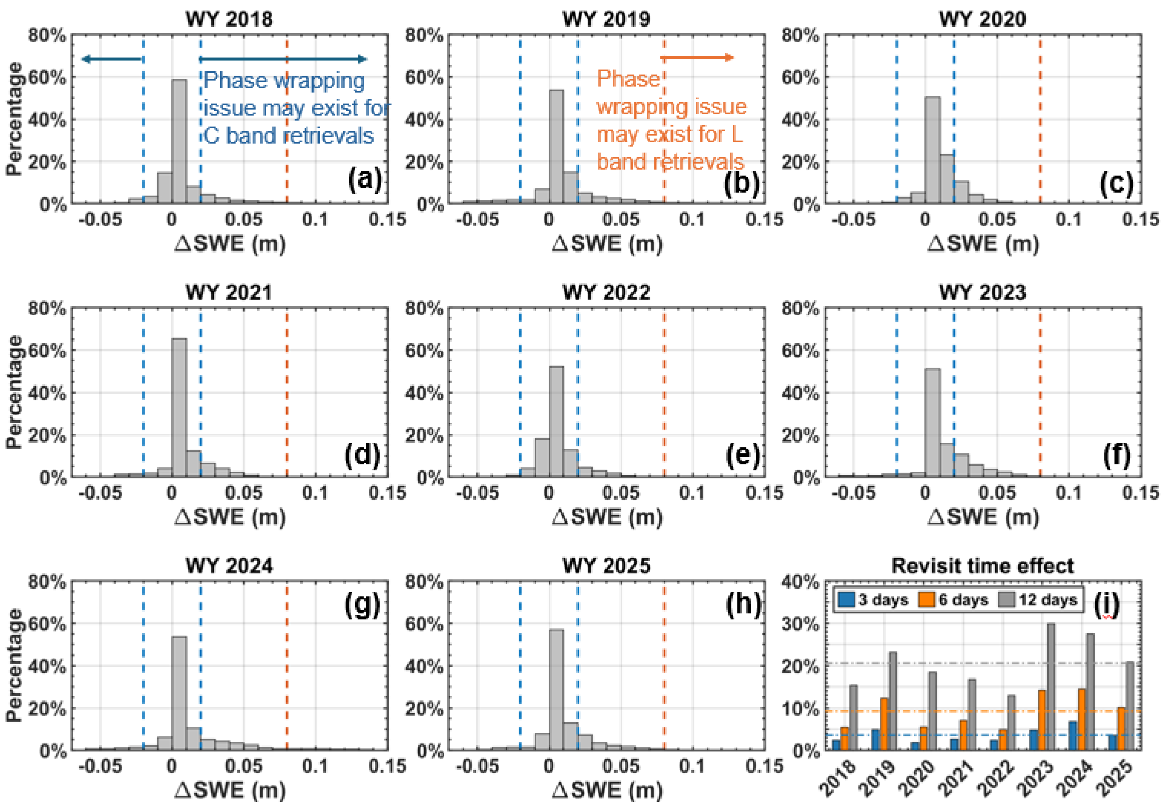

Figure 8: Panel (a) to (h) show the histogram of 12-day pixel-wise ΔSWE distributions at the Kelan watershed over WYs 2018 to 2025. Pixel-time samples with the absolute value of ΔSWE > 0.02 m (beyond the blue dashed lines) are susceptible to phase wrapping in C-band measurement pairs. Pixel-time samples with ΔSWE > 0.08 m (beyond the red dashed line) are susceptible to phase wrapping in L-band
365 measurement pairs. Panel (i) summarized the percentage of pixel-time with ΔSWE > 0.02 m over 8 years across revisit intervals of 3 days (blue), 6 days (orange), and 12 days (gray). The horizontal lines show the 8-year averaged percentage of pixel-time with ΔSWE > 0.02 m for three revisit intervals.

Higher elevations with deeper snowpack exhibit more pixel-time samples in which ΔSWE exceeds 0.02 m as illustrated in Fig. 9c. For elevations above 1250 m, the 8-year median probability of observing 12-day ΔSWE values greater than 0.02 m is above
370 20 %. The percentage of median probability gets doubled at elevations above 2500 m, where stores over 25% of the snow water volumes. The minimum likelihood is still above 30% at elevations above 2500 m, suggesting that a significant proportion of pixel-time samples are likely require phase unwrapping during C-band InSAR retrieval. Notably, even at low elevational

https://doi.org/10.5194/egusphere-2026-5345
Preprint. Discussion started: 23 September 2026

bands, the median likelihood remains substantial (>10% for most cases), underscoring the need to address phase wrapping across all elevational bands. Reducing the revisit time from 12 to 6 or 3 days reduces the likelihood of observing ΔSWE values exceeding 0.02 m across all elevation bands. Similar to the findings in Fig. 8i, even with a 3-day revisit interval, up to 10% of C-band satellite observation pairs are likely to experience phase wrapping issue at elevations above 2500 m.

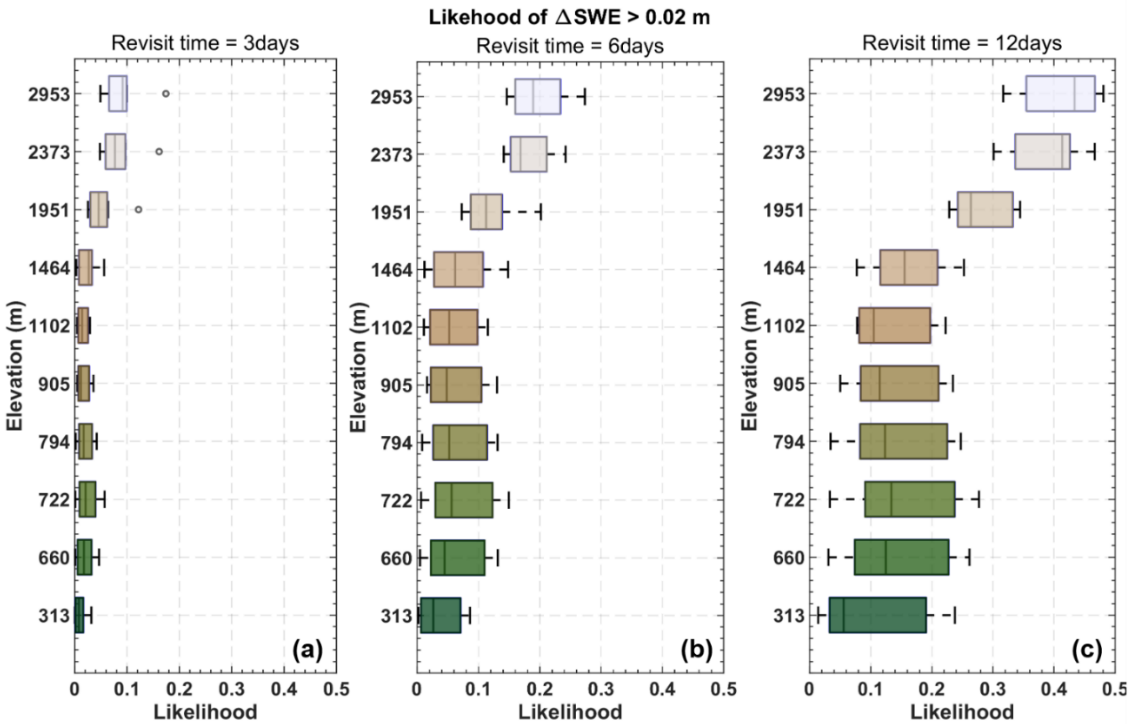

Figure 9: Elevational distribution of likelihood of ΔSWE > 0.02 m over 8 years across revisit time of 3 days, 6 days, and 12 days.

3.4 Evaluation of InSAR derived products based on the snow reanalysis data

The snow reanalysis data obtained by assimilating HLS fSCA (hereafter snow reanalysis) are used as a reference to detect the likelihood of phase-wrapping issues in the InSAR ΔSWE retrievals in the Kelan watershed. The snow reanalysis dataset is further used to adjust the InSAR-derived ΔSWE and as a baseline to evaluate the effect of assimilating adjusted InSAR ΔSWE. If the difference between the InSAR and snow reanalysis ΔSWE is more than one 2π wrapping cycle, the original InSAR ΔSWE is additionally adjusted by integer numbers of wrapping cycles using Eq. 6 to align with the snow reanalysis data.

Although Zhou et al. (2025) bias-corrected the phase parameters by calibrating the integer multiple of 2π and its residuals using in situ points, phase wrapping issue remains (Fig. 10) in ΔSWE derived from Sentinel-1 C-band wrapping pairs. Comparing with the snow reanalysis ΔSWE, in WY 2020, at least six measurement days have phase wrapping issue affecting over 15% of pixels. For each measurement day, the percentage of pixels that may be affected by phase wrapping can be as high as 80% between 15 Mar 2020 – 27 Mar 2020. During this period, the InSAR derived data show a domain-wide increase

https://doi.org/10.5194/egusphere-2026-5345
Preprint. Discussion started: 23 September 2026

of SWE, whereas snow reanalysis data exhibits modest SWE accumulation at high elevations and SWE melt at elevations below 1500 m. Due to the disagreement between the two datasets, more than 40% of InSAR ΔSWE values are adjusted by over 2 phase wrapping cycles over these two days to match snow reanalysis data.

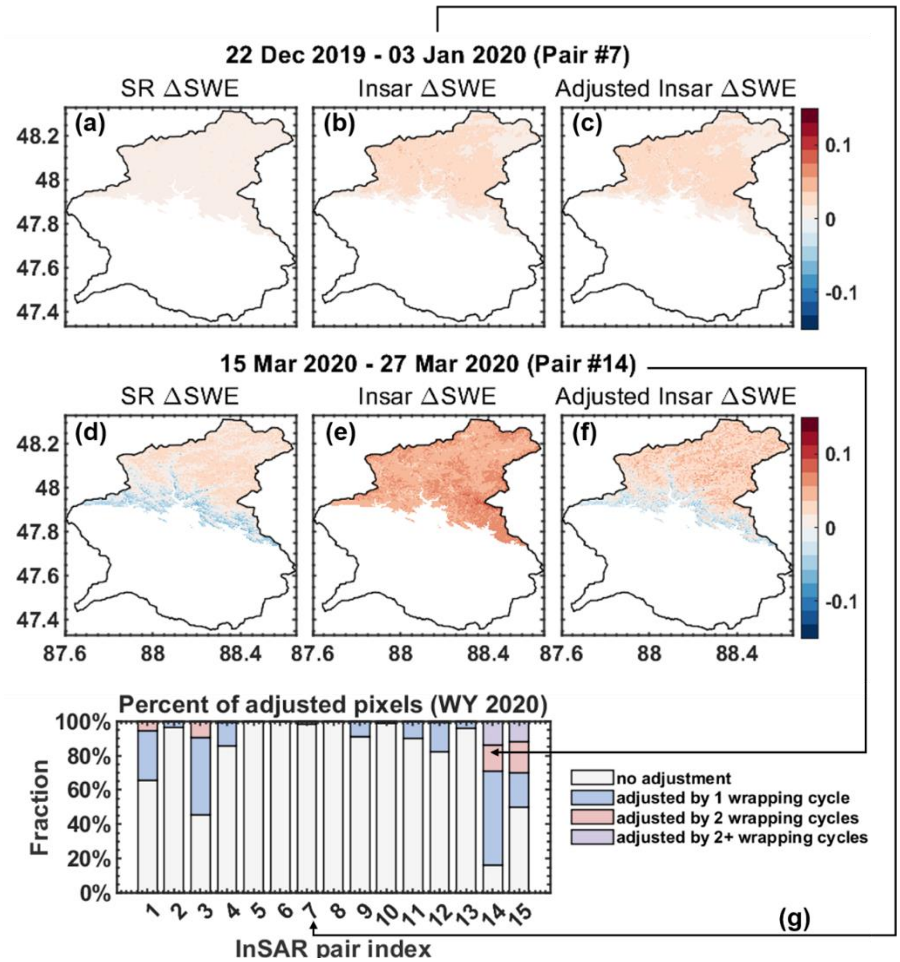

Figure 10: Spatial map of snow reanalysis (SR), original InSAR ΔSWE retrievals, and adjusted InSAR ΔSWE on 22 Dec 2019 – 03 Jan 2020 (a-c), and 15 Mar 2020 – 27 Mar 2020 (d-f) at the Kelan watershed with elevation above 1250 m. Panel (g) shows the percentage of pixels without adjustment, adjusted by 1, 2, and 2+ wrapping cycles. The dates for interval index in WY 2020 are listed in Table 1. One wrapping cycle represents that ΔSWE needs to be adjusted by one 2π wrapping cycle to align with the reanalysis reference.

Figure 11 illustrates that the occurrence of phase wrapping in WY 2020 is related to the coherence and topography including elevation and slope. For pixel-time samples with coherence < 0.3 (Fig.11 e), as high as 30% of them tends to have phase ambiguity issue. The percentage drops substantially to less than 5% for pixel-time sample with coherences > 0.8. High-elevation pixels (i.e., above 1500 m) predominantly require one 2π wrapping cycle to align with the reanalysis reference among adjusted samples. In contrast, at low-elevation pixels, affected samples are distributed more evenly across

https://doi.org/10.5194/egusphere-2026-5345
Preprint. Discussion started: 23 September 2026

1, 2, and 2+ wrapping cycles (each ~5%). As confirmed in Fig. 12 (c), samples with 2+ wrapping cycles adjustments are located at lower elevations. These cases happen in the last two measurement periods, 15 Mar 2020 - 27 Mar 2020 and 27 Mar 2020 - 08 Apr 2020 (Fig. 10g), when inconsistent changes of SWE are observed between the snow reanalysis data and the unadjusted InSAR data at low elevation. The percentage of pixel-time samples requiring adjustment is consistent across slope bins, although steeper slopes have a relatively higher proportion of samples adjusted by 2 or more wrapping cycles. The percentage of adjustment show no significant association with vegetation coverage and terrain aspect, suggesting that the residual phase wrapping issue in InSAR ΔSWE retrieval is not strongly influenced by either factor.

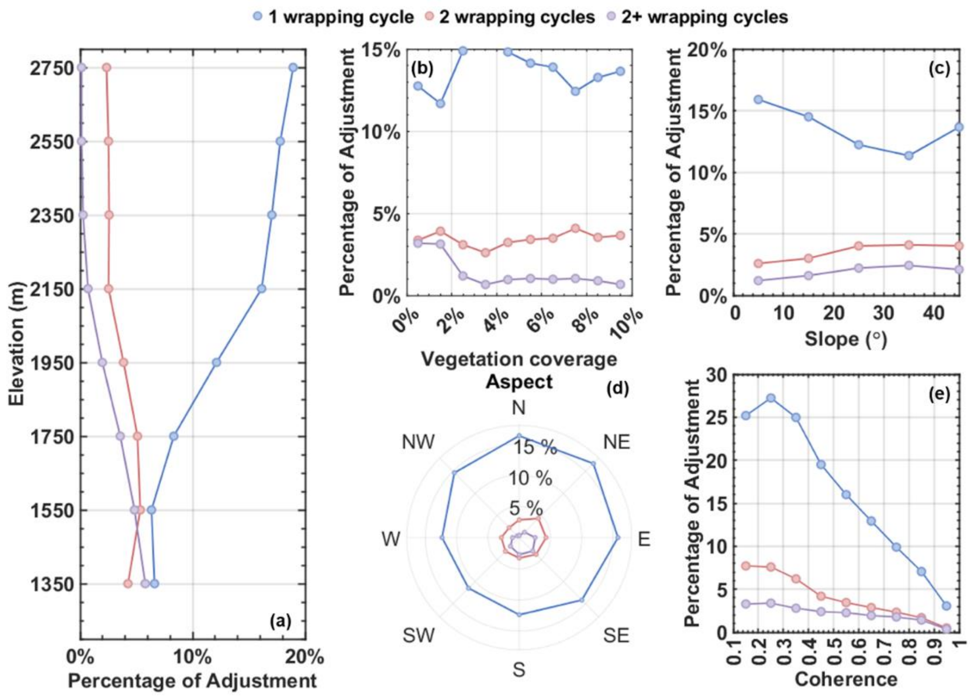

Figure 11: The occurrence in percentage of pixel-time adjusted by 1 wrapping phase, 2 wrapping phase, and 2+ wrapping phase among all measurement pixels and times over various elevation (a), vegetation coverages (b), slopes (c), aspect (d), and coherence bins (e) in WY 2020.

Among all measurement periods, the average percentage of time when Sentinel-1 ΔSWE is one wrapping cycle away from the snow reanalysis is ~14 % (~2 out of 15 measurement pairs) and 11 % (~2 out of 17 measurement pairs) in WY 2020 and 2021, respectively (Fig. 12). Pixels with a percentage of adjustment greater than 20 % (more than 4 measurement pairs) are visually noticeable in both WYs 2020 and 2021. In WY 2024, LuTan-1 L-band observations are available only during the snow compaction season, when the SWE changes between consecutive acquisitions remain below one L-band phase cycle (< ~80 mm). The phase wrapping in this year is negligible, affecting fewer than 2 % of pixel-time samples.

https://doi.org/10.5194/egusphere-2026-5345
Preprint. Discussion started: 23 September 2026

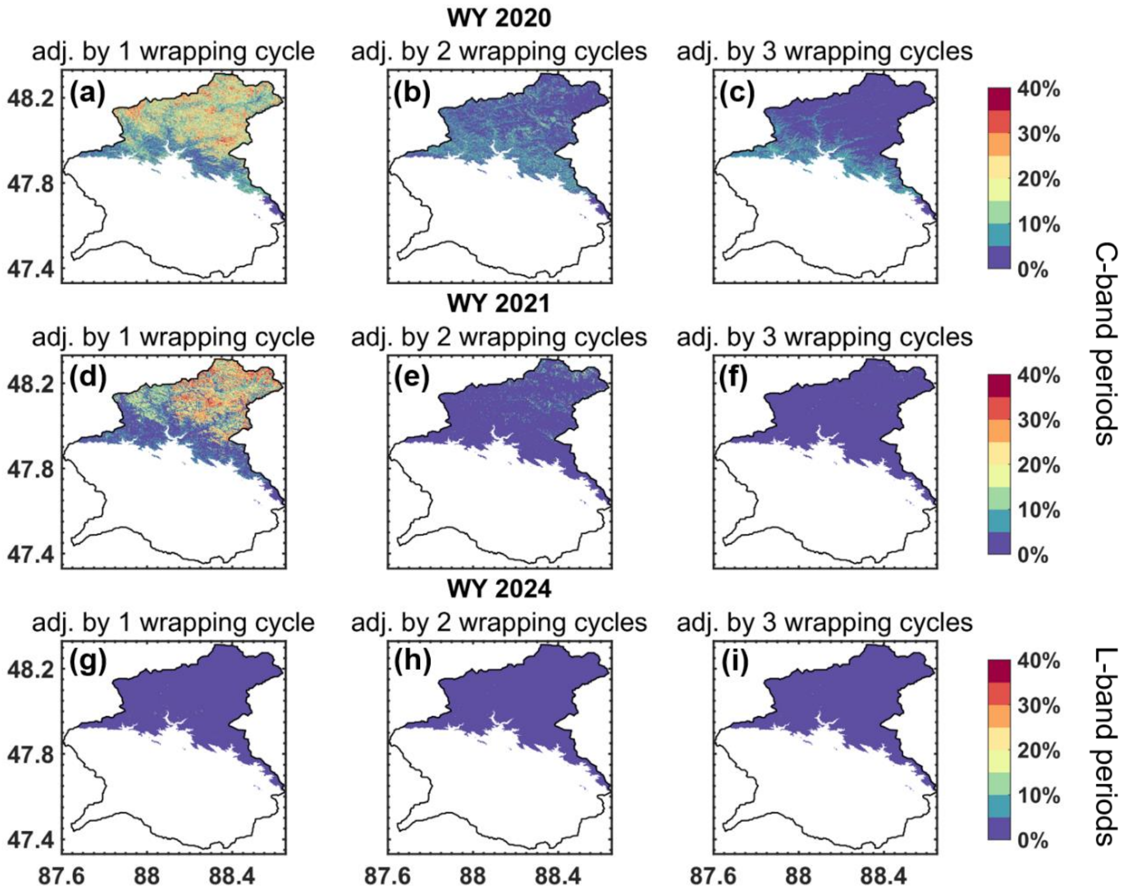

420 **Figure 12:** Percent of all measurement time with ΔSWE adjusted by 1 phase cycle (left panels), 2 phase cycles (middle panels), and more than 2 phase cycles (right panels) at all pixels above 1250 m at the Kelan watershed over WY 2020 (a-c), 2021 (d-e), 2024 (f-g).

3.5 Impact of phase wrapping issues on SWE estimates via data assimilation

At the WXLK station, the uRMSD between the in situ ΔSWE measurements and InSAR ΔSWE retrievals across all pairs is ~ 0.017 m, 0.019 m, and 0.007 m, in WY 2020 (C band), 2021 (C band), and 2024 (L band). Including only measurement pairs with InSAR coherence > 0.8 reduces the uRMSD to ~ 0.011 m in WY 2020 and 0.015 m in WY 2021. The statistics remain unchanged in WY 2024 because no adjustment of ΔSWE measurements is required. The potential error caused by phase wrapping issue is detected at the in situ site in the Sentinel-1 C-band retrieved ΔSWE product in WY 2020. As shown in Fig. 13a, InSAR derived data fairly capture the changes in SWE at most of the measurement dates with coherence above 0.8. However, from 15 Mar to 27 Mar 2020, InSAR derived ΔSWE from Sentinel-1C is overpredicted by approximately 0.034 m relative to ΔSWE computed from in situ measurements, roughly corresponding to a 2π phase cycle. Assimilating ΔSWE measurements containing this biased observation results in a higher uRMSD for the posterior than for the prior because higher weights are assigned to ensembles with a large increase in ΔSWE during this period. Using snow

https://doi.org/10.5194/egusphere-2026-5345
Preprint. Discussion started: 23 September 2026

reanalysis ΔSWE as a reference, the adjusted InSAR ΔSWE from 15 Mar to 27 Mar 2020 is much closer to the in situ measurement. In contrast, the adjusted InSAR ΔSWE from 27 Mar 2020 - 08 Apr 2020 exhibits a larger negative bias relative to the in situ measurements compared with the original InSAR data. It indicates that snow reanalysis SWE decreases faster than the in situ measurement during this period, potentially causing an improper adjustment. After the assimilation of adjusted InSAR ΔSWE with coherence above 0.8, daily posterior SWE estimates are improved by 31 % with uRMSD of 0.029 m from the prior. The uRMSD statistics are comparable to the results with the assimilation of fSCA in WY 2020 at WXLK site. Note that prior statistics from pixel-wise data (Fig. 11) are slightly different from the domain-wide data (Fig.2) due to random seed used to generate the data. By relaxing the coherence constraint from 0.8 to 0.5, daily posterior SWE are improved by 52 % with uRMSD of 0.020 m. Both prior and posterior snow depth estimate have low and comparable uRMSD compared to the in situ measurements. Figure S5 shows that uRMSD of 0.034 m in daily SWE in WY 2021 remains comparable with the snow reanalysis data. In contrast, the uRMSD of 0.100 m is higher in WY 2024 (Fig. S6) by assimilating LuTan-1 L-band ΔSWE retrieval than the baseline snow reanalysis data with an uRMSD of 0.051 m (Fig. 2f), partially because high-quality InSAR ΔSWE is only available during snow compaction season when limited ΔSWE information is available to update SWE.

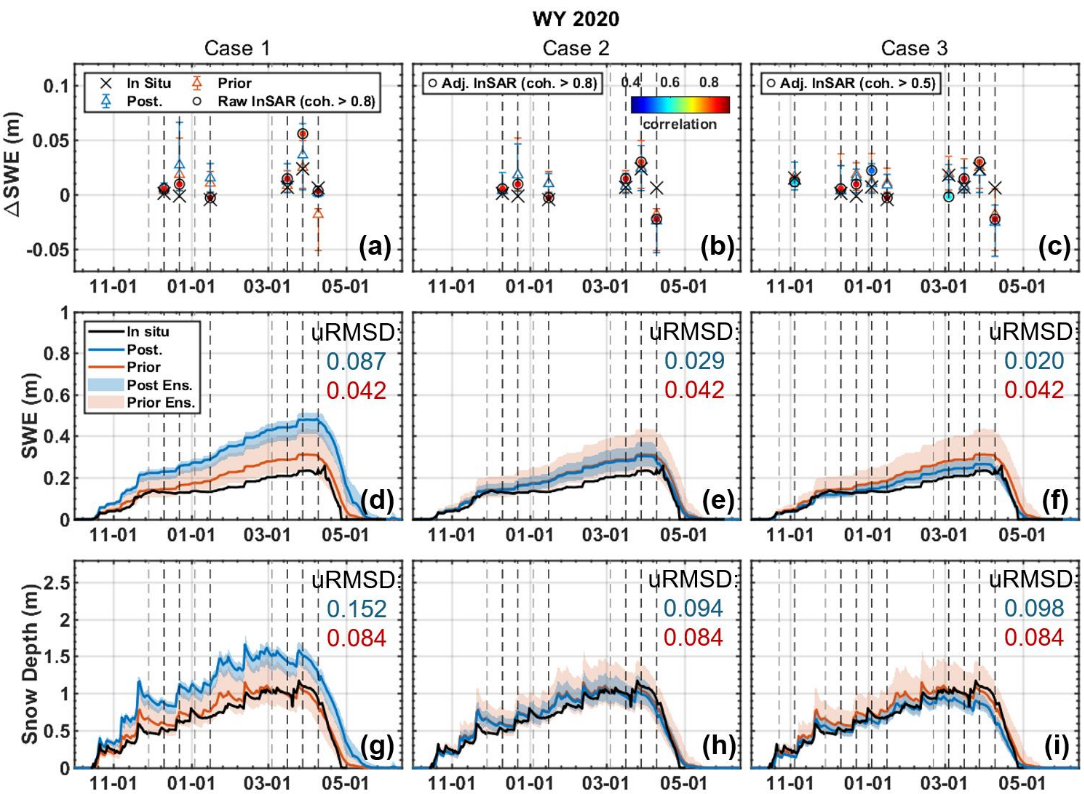

Figure 13: Time series of prior, posterior, and measured ΔSWE (a-c), SWE (d-f), and snow depth (g-i) in meters over WY 2020 at the WXLK site. ΔSWE computed from in situ SWE is marked as 'x' marks in panels (a) and (d). Vertical dashed lines are Sentinel-1 InSAR

https://doi.org/10.5194/egusphere-2026-5345
Preprint. Discussion started: 23 September 2026

observation dates. The left panels are results with the assimilation of all selected InSAR ΔSWE measurements. The middle panels and right panels are are results with the assimilation of adjust InSAR ΔSWE with coherence > 0.5 and 0.8, respectively.

At elevations above 1250 m, 2000 pixels are randomly selected to analyze the effect of assimilation of InSAR derived ΔSWE. The prior and posterior data after assimilation are compared against the baseline snow reanalysis data. Overall, assimilation of InSAR derived ΔSWE using the current PBS method yields improvement in SWE estimates in around half of cases (Fig. 14). Compared to the snow reanalysis SWE, assimilation of adjusted InSAR ΔSWE with coherence > 0.5 shows modest improvement compared to assimilation of raw InSAR ΔSWE. The uRMSD of posterior ΔSWE is reduced by more than 10 % from the prior for around 48% of pixels, after assimilation of unadjusted InSAR derived ΔSWE. The percentage increases to ~56 % of pixels with the assimilation of adjusted ΔSWE in WY 2020. In WY 2021, the uRMSD is reduced by more than 10 % from the prior to the posterior for ~ 36 %, 40 %, 42 % of pixels after assimilation of original InSAR ΔSWE with coherence >0.8, adjusted ΔSWE with coherence > 0.8, and adjusted ΔSWE with coherence > 0.5, respectively. In WY 2024, the improvement of posterior SWE compared to the prior is comparable using original or adjusted InSAR ΔSWE with coherence > 0.8 due to negligible phase wrapping issue in L-band. Around 47 % of pixels show an improvement in posterior SWE compared to the prior with the assimilation of InSAR derived ΔSWE. With the assimilation of adjusted ΔSWE observations with coherence > 0.5, the percentage of pixels exhibiting a decrease of more than 10 % in uRMSD from prior to posterior SWE increases to ~ 53 %.

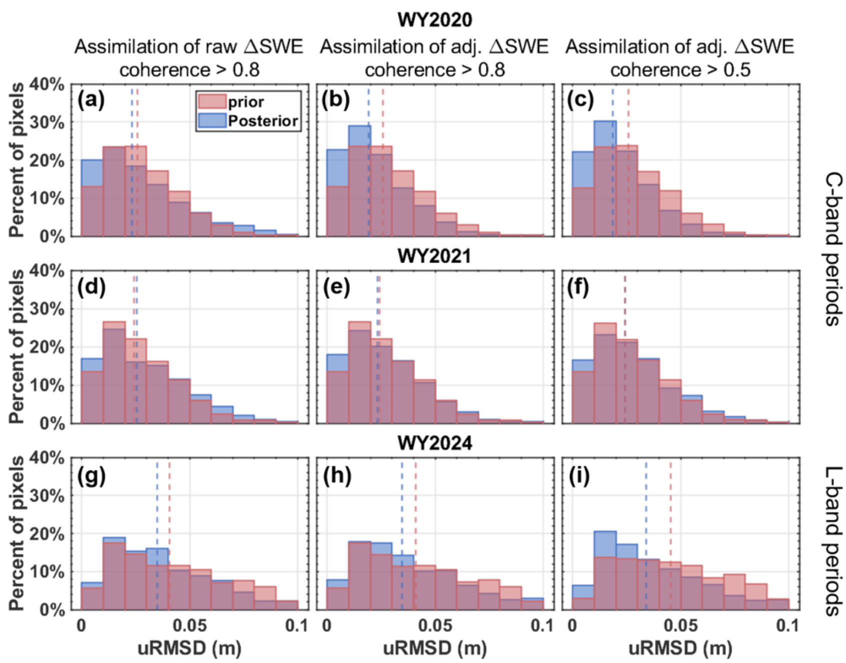

Figure 14: Histogram of posterior and prior uRMSD in three scenarios: 1) assimilation of original InSAR derived ΔSWE with coherence > 0.8 (left panels); 2) assimilation of adjusted ΔSWE (middle panels) with coherence > 0.8; 3) assimilation of adjusted ΔSWE with coherence >

https://doi.org/10.5194/egusphere-2026-5345
Preprint. Discussion started: 23 September 2026

0.5 (right panels) over WY 2020 (a-c), 2021 (d-i), and 2024 (g-i). The ΔSWE measurements in WY 2020, and 2021 are retrieved from Sentinel-1 C-band products. The ΔSWE measurements in WY 2024 are retrieved from LuTan-1 L-band products. The vertical dashed line represents median uRMSD in prior (red) and posterior (blue).

4. Conclusion and future work

This work generated an 8-year (WYs 2018 to 2025) daily SWE dataset at the Kelan watershed, Altay, by assimilating retrieved fSCA from Harmonized Landsat 8/9 and Sentinel-2A/B satellites at a spatial resolution of ~150 m. Verification of SWE against the WXLK in situ site shows uRMSD values of 0.025, 0.031, 0.051 m in WYs 2020, 2021, and 2024, respectively, roughly corresponding to approximately 10 % of peak SWE. Among the study water years, the maximum peak SWE volume is ~1.16 km^3 in WY 2024, whereas the minimum peak SWE volume is ~ 0.56 km^3 in WY 2021. Over a quarter of the total snow water is stored above ~2500 m, corresponding to 10% of the total area where in situ measurements are typically not available. Verification against in situ snow depth data shows that the 33-site average relative uRMSD percentage is ~9 % and relative MD percentage is ~ 3 % of the peak in situ snow depth in WY 2025. The posterior estimates fairly capture the spatial distribution of snow depth compared against the Lidar swath measurements. This dataset can be used as a benchmark for evaluating new snow products at the Kelan watershed when in situ measurements are not available.

The generated snow reanalysis is used to characterize the likelihood of phase ambiguity and to assess the value of InSAR derived ΔSWE for constraining SWE. Analysis of the 2018-2025 snow reanalysis dataset indicates that SWE increases by more than 0.02-0.03 m (corresponding to a 2π wrapping cycle in C band) over a 12-day period in ~20% or more of the pixel-time samples in most of the years, likely to have phase wrapping issue in C-band InSAR retrievals. The likelihood is reduced to less than 2% for L-band retrievals between 12-day measurement periods. Compared with the reanalysis data, residual phase unwrapping issue exists in the newly developed InSAR ΔSWE product from Sentinel-1 C band measurements in the study domain. Screening out ΔSWE measurements with coherence less than 0.8 reduces the average number of measurements affected by phase wrapping to 1 out of 7 days at each pixel. However, assimilation of measurements containing a single erroneous ΔSWE measurement can substantially impact the accuracy of SWE estimates over the whole WY using the PBS method. At the WXLK site, assimilation of adjusted C-band InSAR ΔSWE measurement yields comparable performance of posterior SWE estimates compared to the baseline reanalysis dataset in WY 2020 and 2021. Although no phase-wrapping issue was found in L-band measurements in WY 2024 at the WXLK site, InSAR ΔSWE retrievals are only available during snow compaction season, providing limited information to update SWE estimates. Among 2000 randomly selected pixels at elevations above 1250 m, assimilation of C-band and L-band InSAR retrieved ΔSWE shows limited effectiveness in improving SWE estimates using fSCA as a baseline. This is partly related to the scarcity of high-quality InSAR observations compared to fSCA observations, Sentinel-1's relatively long revisit interval, the restriction of LuTan-1 ΔSWE retrievals primarily to low-accumulation days, and the possibility that the used data assimilation approach was not ideally suited to ΔSWE observations.

https://doi.org/10.5194/egusphere-2026-5345
Preprint. Discussion started: 23 September 2026

Overall, residual phase wrapping issues remain in InSAR ΔSWE retrieved from the Sentinel-1 C band in the Kelan watershed, which substantially affect the accuracy of SWE estimates after assimilation. Future experiments may use synthesized observing system simulation experiments (OSSEs) to isolate the benefits of ΔSWE observations for data assimilation and quantify the effects of phase-unwrapping errors on reanalysis performance. Additionally, assimilation approaches that can directly account for phase-cycle uncertainty in C-band retrievals need to be developed and evaluated. Due to the limited available InSAR ΔSWE measurements from L-band in the Kelan watershed, this manuscript does not comprehensively address the use of L-band measurements to constraining SWE. Measurements acquired under wet snow conditions need further evaluation. A forward snow microwave model can be useful to study the impact of snow water content, forest coverage, and topography on phase delays and their contribution to retrieval uncertainties in phase changes.

Beyond the technical advancements in Altay Mountain SWE estimates explored in this study, a critical future research direction lies in quantifying the impacts of climate change on the regional economy through the snow-water pathway and providing evidence-based insights to inform climate adaptation policies in the Altay prefecture. This study can extend the dataset to the Landsat era (since 1985) and integrate it with regional economic statistics and sectoral water demand models to conduct a coupled climate-snow-water-economy impact assessment based on historical data. Future research in Altay and analogous mountainous regions of northwestern China can further focus on scenario-based modeling to evaluate the economic vulnerability of key sectors under different climate change trajectories (e.g., moderate vs. high warming scenarios) and identify critical thresholds of SWE change (e.g., shifts in peak SWE volume, earlier melt-out dates, and uneven elevational snow distribution) that trigger significant economic risks. This vulnerability assessment will lay the foundation for designing targeted climate adaptation policies, such as optimized water resource allocation strategies for primary production, adaptive planning for snow tourism infrastructure (e.g., adjusting operating seasons based on projected snow phenology), and the development of early warning systems for snowmelt-driven water scarcity or flood risks.

Data availability

The 8-year snow reanalysis data generated for the Kelan watershed through the assimilation of fractional snow covered area retrieved from the Harmonized Landsat and Sentinel data is publicly available on https://doi.org/10.6084/m9.figshare.33421588.

Supplement

The supplement related to this article is available in the submitted supplement.

https://doi.org/10.5194/egusphere-2026-5345
Preprint. Discussion started: 23 September 2026

Author contributions

YF contributed to the conceptualization, data curation, formal analysis, funding acquisition, methodology, visualization, and writing. JP contributed to the conceptualization, data resources, review, and editing. SM contributed to the conceptualization, reanalysis code resources, and review. JZ contributed to the data preparation and review. HS contributed to reanalysis code resources, review and editing. YL contributed to funding acquisition and review. CX contributed to review and editing. HW contributed to review and editing. ST contributed to conceptualization, supervision, funding acquisition, review and editing.

Competing interests

The contact author has declared that neither of the authors has any competing interests.

Disclaimer

Copernicus Publications remains neutral with regard to jurisdictional claims made in the text, published maps, institutional affiliations, or any other geographical representation in this paper. While Copernicus Publications makes every effort to include appropriate place names, the final responsibility lies with the authors. Views expressed in the text are those of the authors and do not necessarily reflect the views of the publisher.

Financial support

This work was funded by the National Key Research and Development Program of China under Grants 2022YFB3903300 and 2022YFB3903303, the National Natural Science Foundation of China (NSFC) under Grant No.42601582, the Zhejiang University startup funds and the Haining Chaoyong Program.

References

Aizen, V. B., Aizen, E. M., Joswiak, D. R., Fujita, K., Takeuchi, N., and Nikitin, S. A.: Climatic and atmospheric circulation pattern variability from ice-core isotope/geochemistry records (Altai, Tien Shan and Tibet), Annals of Glaciology, 43, 49–60, https://doi.org/10.3189/172756406781812078, 2006.

Bair, E. H., Stillinger, T., and Dozier, J.: Snow Property Inversion From Remote Sensing (SPIReS): A Generalized Multispectral Unmixing Approach With Examples From MODIS and Landsat 8 OLI, IEEE Transactions on Geoscience and Remote Sensing, 59, 7270–7284, https://doi.org/10.1109/TGRS.2020.3040328, 2021.

https://doi.org/10.5194/egusphere-2026-5345
Preprint. Discussion started: 23 September 2026

Besso, H., Shean, D., and Lundquist, J. D.: Mountain snow depth retrievals from customized processing of ICESat-2 satellite laser altimetry, Remote Sensing of Environment, 300, 113843, https://doi.org/10.1016/j.rse.2023.113843, 2024.

Claverie, M., Ju, J., Masek, J. G., Dungan, J. L., Vermote, E. F., Roger, J.-C., Skakun, S. V., and Justice, C.: The Harmonized Landsat and Sentinel-2 surface reflectance data set, Remote Sensing of Environment, 219, 145–161, https://doi.org/10.1016/j.rse.2018.09.002, 2018.

Cortés, G. and Margulis, S.: Impacts of El Niño and La Niña on interannual snow accumulation in the Andes: Results from a high-resolution 31 year reanalysis, Geophysical Research Letters, 44, 6859–6867, https://doi.org/10.1002/2017GL073826, 2017.

Dai, L., Che, T., Zhang, Y., Ren, Z., Tan, J., Akynbekkyzy, M., Xiao, L., Zhou, S., Yan, Y., Liu, Y., Li, H., and Wang, L.: Microwave radiometry experiment for snow in Altay, China: time series of in situ data for electromagnetic and physical features of snowpack, Earth System Science Data, 14, 3509–3530, https://doi.org/10.5194/essd-14-3509-2022, 2022.

Fang, Y., Liu, Y., and Margulis, S. A.: A western United States snow reanalysis dataset over the Landsat era from water years 1985 to 2021, Sci Data, 9, 677, https://doi.org/10.1038/s41597-022-01768-7, 2022.

Farr, T. G., Rosen, P. A., Caro, E., Crippen, R., Duren, R., Hensley, S., Kobrick, M., Paller, M., Rodriguez, E., Roth, L., Seal, D., Shaffer, S., Shimada, J., Umland, J., Werner, M., Oskin, M., Burbank, D., and Alsdorf, D.: The Shuttle Radar Topography Mission, Reviews of Geophysics, 45, https://doi.org/10.1029/2005RG000183, 2007.

Gelaro, R., McCarty, W., Suárez, M. J., Todling, R., Molod, A., Takacs, L., Randles, C. A., Darmenov, A., Bosilovich, M. G., Reichle, R., Wargan, K., Coy, L., Cullather, R., Draper, C., Akella, S., Buchard, V., Conaty, A., Silva, A. M. da, Gu, W., Kim, G.-K., Koster, R., Lucchesi, R., Merkova, D., Nielsen, J. E., Partyka, G., Pawson, S., Putman, W., Rienecker, M., Schubert, S. D., Sienkiewicz, M., and Zhao, B.: The Modern-Era Retrospective Analysis for Research and Applications, Version 2 (MERRA-2), https://doi.org/10.1175/JCLI-D-16-0758.1, 2017.

Global Modeling and Assimilation Office (GMAO): tavg1_2d_flx_Nx: MERRA-2 2d,1-Hourly,Time-Averaged,Single-Level,Assimilation,Surface Flux Diagnostics 0.625 x 0.5 degree V5.12.4, https://doi.org/10.5067/7MCPBJ41Y0K6, 2015a.

Global Modeling and Assimilation Office (GMAO): tavg1_2d_rad_Nx: MERRA-2 2d,1-Hourly,Time-Averaged,Single-Level,Assimilation,Radiation Diagnostics V5.12.4, https://doi.org/10.5067/Q9QMY5PBNV1T, 2015b.

Global Modeling and Assimilation Office (GMAO): tavg1_2d_slv_Nx: MERRA-2 2d,1-Hourly,Time-Averaged,Single-Level,Assimilation,Single-Level Diagnostics 0.625 x 0.5 degree V5.12.4, https://doi.org/10.5067/VJAFPLI1CSIV, 2015c.

https://doi.org/10.5194/egusphere-2026-5345
Preprint. Discussion started: 23 September 2026

Guneriussen, T., Hogda, K. A., Johnsen, H., and Lauknes, I.: InSAR for estimation of changes in snow water equivalent of dry snow, IEEE Transactions on Geoscience and Remote Sensing, 39, 2101–2108, https://doi.org/10.1109/36.957273, 2001.

Hansen, M. C., Defries, R. S., Townshend, J. R. G., and Sohlberg, R.: Global land cover classification at 1 km spatial resolution using a classification tree approach, International Journal of Remote Sensing, 21, 1331–1364, https://doi.org/10.1080/014311600210209, 2000.

Hoppinen, Z., Oveisgharan, S., Marshall, H.-P., Mower, R., Elder, K., and Vuyovich, C.: Snow water equivalent retrieval over Idaho – Part 2: Using L-band UAVSAR repeat-pass interferometry, The Cryosphere, 18, 575–592, https://doi.org/10.5194/tc-18-575-2024, 2024.

Hu, X., Hao, X., Wang, J., Huang, G., Li, H., and Yang, Q.: Can the Depth of Seasonal Snow be Estimated From ICESat-2 Products: A Case Investigation in Altay, Northwest China, IEEE Geoscience and Remote Sensing Letters, 19, 1–5, https://doi.org/10.1109/LGRS.2021.3078805, 2022.

Kobayashi, S., Ota, Y., Harada, Y., Ebita, A., Moriya, M., Onoda, H., Onogi, K., Kamahori, H., Kobayashi, C., Endo, H., Miyaoka, K., and Takahashi, K.: The JRA-55 Reanalysis: General Specifications and Basic Characteristics, Journal of the Meteorological Society of Japan. Ser. II, 93, 5–48, https://doi.org/10.2151/jmsj.2015-001, 2015.

Leinss, S., Wiesmann, A., Lemmetyinen, J., and Hajnsek, I.: Snow Water Equivalent of Dry Snow Measured by Differential Interferometry, IEEE J. Sel. Top. Appl. Earth Observations Remote Sensing, 8, 3773–3790, https://doi.org/10.1109/JSTARS.2015.2432031, 2015.

Lievens, H., Demuzere, M., Marshall, H.-P., Reichle, R. H., Brucker, L., Brangers, I., de Rosnay, P., Dumont, M., Girotto, M., Immerzeel, W. W., Jonas, T., Kim, E. J., Koch, I., Marty, C., Saloranta, T., Schöber, J., and De Lannoy, G. J. M.: Snow depth variability in the Northern Hemisphere mountains observed from space, Nat Commun, 10, 4629, https://doi.org/10.1038/s41467-019-12566-y, 2019.

Liston, G. E.: Representing Subgrid Snow Cover Heterogeneities in Regional and Global Models, 2004.

Liu, Y. and Margulis, S. A.: Deriving Bias and Uncertainty in MERRA-2 Snowfall Precipitation Over High Mountain Asia, Front. Earth Sci., 7, https://doi.org/10.3389/feart.2019.00280, 2019.

Liu, Y., Fang, Y., and Margulis, S. A.: Spatiotemporal distribution of seasonal snow water equivalent in High Mountain Asia from an 18-year Landsat–MODIS era snow reanalysis dataset, The Cryosphere, 15, 5261–5280, https://doi.org/10.5194/tc-15-5261-2021, 2021.

Liu, Y., Fang, Y., Li, D., and Margulis, S. A.: How Well do Global Snow Products Characterize Snow Storage in High Mountain Asia?, Geophysical Research Letters, 49, e2022GL100082, https://doi.org/10.1029/2022GL100082, 2022.

https://doi.org/10.5194/egusphere-2026-5345
Preprint. Discussion started: 23 September 2026

Margulis, S. A., Girotto, M., Cortés, G., and Durand, M.: A Particle Batch Smoother Approach to Snow Water Equivalent Estimation, Journal of Hydrometeorology, 16, 1752–1772, https://doi.org/10.1175/JHM-D-14-0177.1, 2015.

Margulis, S. A., Cortés, G., Girotto, M., and Durand, M.: A Landsat-Era Sierra Nevada Snow Reanalysis (1985–2015), Journal of Hydrometeorology, 17, 1203–1221, https://doi.org/10.1175/JHM-D-15-0177.1, 2016.

Margulis, S. A., Liu, Y., and Baldo, E.: A Joint Landsat- and MODIS-Based Reanalysis Approach for Midlatitude Montane Seasonal Snow Characterization, Front. Earth Sci., 7, https://doi.org/10.3389/feart.2019.00272, 2019.

Margulis, S. A., Hildebrand, M., Xu, X., Girotto, M., Marshall, H.-P., Shah, R., Deeb, E., Yueh, S., Entekhabi, D., and Lundquist, J.: Interferometric synthetic aperture radar (InSAR) phase data assimilation for Bayesian snow water equivalent estimation, EGUsphere, 1–39, https://doi.org/10.5194/egusphere-2026-1594, 2026.

Matzler, C.: Microwave permittivity of dry snow, IEEE Transactions on Geoscience and Remote Sensing, 34, 573–581, https://doi.org/10.1109/36.485133, 1996.

Muñoz-Sabater, J., Dutra, E., Agustí-Panareda, A., Albergel, C., Arduini, G., Balsamo, G., Boussetta, S., Choulga, M., Harrigan, S., Hersbach, H., Martens, B., Miralles, D. G., Piles, M., Rodríguez-Fernández, N. J., Zsoter, E., Buontempo, C., and Thépaut, J.-N.: ERA5-Land: a state-of-the-art global reanalysis dataset for land applications, Earth System Science Data, 13, 4349–4383, https://doi.org/10.5194/essd-13-4349-2021, 2021.

NASA JPL.: NASA Shuttle Radar Topography Mission Global 1 arc second, https://doi.org/https://doi.org/10.5067/MEASURES/SRTM/SRTMGL1.003, 2013.

Oveisgharan, S., Zinke, R., Hoppinen, Z., and Marshall, H. P.: Snow water equivalent retrieval over Idaho – Part 1: Using Sentinel-1 repeat-pass interferometry, The Cryosphere, 18, 559–574, https://doi.org/10.5194/tc-18-559-2024, 2024.

Oveisgharan, S., Havazli, E., Zinke, R., and Hoppinen, Z.: Using LIDAR and SNOTEL Data for Evaluating the Performance of Snow Water Equivalent Retrieval Using Sentinel-1 Repeat-Pass Interferometry, EGUsphere, 1–27, https://doi.org/10.5194/egusphere-2025-5868, 2025.

RGI Consortium: Randolph Glacier Inventory - A Dataset of Global Glacier Outlines, Version 7, https://doi.org/10.5067/F6JMOVY5NAVZ, 2023.

Rodell, M., Houser, P. R., Jambor, U., Gottschalck, J., Mitchell, K., Meng, C.-J., Arsenault, K., Cosgrove, B., Radakovich, J., Bosilovich, M., Entin, J. K., Walker, J. P., Lohmann, D., and Toll, D.: The Global Land Data Assimilation System, https://doi.org/10.1175/BAMS-85-3-381, 2004.

https://doi.org/10.5194/egusphere-2026-5345
Preprint. Discussion started: 23 September 2026

Sexton, J. O., Song, X.-P., Feng, M., Noojipady, P., Anand, A., Huang, C., Kim, D.-H., Collins, K. M., Channan, S., DiMiceli, C., and Townshend, J. R.: Global, 30-m resolution continuous fields of tree cover: Landsat-based rescaling of MODIS vegetation continuous fields with lidar-based estimates of error, International Journal of Digital Earth, 6, 427–448, https://doi.org/10.1080/17538947.2013.786146, 2013.

Shrestha, P. and Barros, A. P.: Assimilation of L-band interferometric synthetic aperture radar (InSAR) snow depth retrievals for improved snowpack quantification, The Cryosphere, 19, 2895–2911, https://doi.org/10.5194/tc-19-2895-2025, 2025.

Shufen, S. and Yongkang, X.: Implementing a new snow scheme in Simplified Simple Biosphere Model, Adv. Atmos. Sci., 18, 335–354, https://doi.org/10.1007/BF02919314, 2001.

Smith, M. O., Ustin, S. L., Adams, J. B., and Gillespie, A. R.: Vegetation in deserts: I. A regional measure of abundance from multispectral images, Remote Sensing of Environment, 31, 1–26, https://doi.org/10.1016/0034-4257(90)90074-V, 1990.

Townshend, J.: Global Forest Cover Change (GFCC) Tree Cover Multi-Year Global 30 m V003, https://doi.org/https://doi.org/10.5067/MEASURES/GFCC/GFCC30TC.003, 2016.

U.S. Geological Survey: Advanced Very High Resolution Radiometer (AVHRR)., https://doi.org/https://doi.org/10.5066/F7K35S5K, 2017.

Wiesmann, A. and Mätzler, C.: Microwave Emission Model of Layered Snowpacks, Remote Sensing of Environment, 70, 307–316, https://doi.org/10.1016/S0034-4257(99)00046-2, 1999.

Xiong, C., Shi, J., Pan, J., Xu, H., Che, T., Zhao, T., Ren, Y., Geng, D., Chen, T., Jiang, K., and Feng, P.: Time Series X- and Ku-Band Ground-Based Synthetic Aperture Radar Observation of Snow-Covered Soil and Its Electromagnetic Modeling, IEEE Transactions on Geoscience and Remote Sensing, 60, 1–13, https://doi.org/10.1109/TGRS.2021.3071373, 2022.

Yang, X., Chen, J., Wang, F., and Chen, Q.: Ice and snow tourism in China's ecological civilization era: The Altay, Xinjiang experience, Habitat International, 159, 103375, https://doi.org/10.1016/j.habitatint.2025.103375, 2025.

Yang, Y., Wu, X.-J., Liu, S.-W., Xiao, C.-D., and Wang, X.: Valuating service loss of snow cover in Irtysh River Basin, Advances in Climate Change Research, 10, 109–114, https://doi.org/10.1016/j.accre.2019.06.004, 2019.

You, Y., Huang, C., Hou, J., Zhang, Y., Wang, Z., and Zhu, G.: Improving the estimation of snow depth in the Noah-MP model by combining particle filter and Bayesian model averaging, Journal of Hydrology, 617, 128877, https://doi.org/10.1016/j.jhydrol.2022.128877, 2023.

https://doi.org/10.5194/egusphere-2026-5345
Preprint. Discussion started: 23 September 2026

Zhang, D., Yang, Y., and Lan, B.: Climate variability in the northern and southern Altai Mountains during the past 50 years, Sci Rep, 8, 3238, https://doi.org/10.1038/s41598-018-21637-x, 2018.

Zhang, Y., Fattahi, H., and Amelung, F.: Small baseline InSAR time series analysis: Unwrapping error correction and noise reduction, Computers & Geosciences, 133, 104331, https://doi.org/10.1016/j.cageo.2019.104331, 2019.

Zhou, J., Lei, Y., Pan, J., Liang, C., Zhang, Y., Li, W., Xiong, C., and Shi, J.: Snow Water Equivalent Retrieval and Analysis Over Altay Using 12-Day Repeat-Pass Sentinel-1 Interferometry, https://doi.org/10.5194/egusphere-2025-2329, 11 June 2025., 2025.